Mon. Not. R. Astron. Soc. **269**, 493–511 (1994)

Tree code simulations of planetary rings

Derek C. Richardson*

Former address: University of Cambridge, Institute of Astronomy, Madingley Road, Cambridge CB3 0HA
Present address: CITA, University of Toronto, 60 St George St, Toronto, Ontario, M5S 1A7, Canada

Accepted 1994 March 11. Received 1993 May 26

ABSTRACT

A tree code method that incorporates a local shearing disc model and fourth-order integration algorithm is applied to the problem of planetary rings, with particular emphasis on the dynamics of Saturn's B ring. The new code, described in detail elsewhere, allows for particle self-gravity, a distribution of particle sizes, and surface friction (particle spin). Important changes made to the original code, to ensure an accurate treatment of collisions under severe high-density conditions, are described in detail. Comparison with work by Wisdom & Tremaine for the case of equal-size particles and mean self-gravity shows excellent agreement. Similar analysis is performed for the new regimes of self-gravity and particle size distributions, and it is shown that the condition for viscous instability is still not satisfied for these models. Particle spins lie generally within a rotational energy equipartition envelope, and are retrograde on average in the rotating (orbital) frame but exhibit a large spread in obliquity. The mean z-directed spin in the fixed frame for most models varies between about 0.2 and 0.4 times the orbital angular velocity, similar to the 0.3 value found by Araki for the equal-size case, while the x and y spin components are generally an order of magnitude smaller. All three spin components have Lorentzian distributions at equilibrium. It is found that aggregates readily form even for conservative size ranges, and the development of gravitational wakes reported by Salo is confirmed. It is proposed that the density variations seen in the models presented, which are the most realistic to date, may account in part for observed non-uniformities in Saturn's outer rings.

Key words: accretion, accretion discs – methods: numerical – celestial mechanics, stellar dynamics – planets and satellites: individual: Saturn – Solar system: formation.

1 INTRODUCTION

It has been recognized for some time that techniques used in numerical simulations of Solar system formation can often be applied to studies of planetary ring dynamics, and vice versa (e.g. Ward 1984). The most important feature common to both systems is a flattened Keplerian disc which describes the mean motion of the constituent particles. These ring particles or planetesimals interact with each other, causing the system to evolve with time to some equilibrium state, or through a series of quasi-equilibrium states. Processes important to both regimes include energy dissipation due to collisions and velocity randomization due to gravitational interactions (Petit & Hénon 1987; Aarseth, Lin & Palmer 1993). Other mechanisms that play a role in these systems include resonance trapping, merging, fragmentation, and gas drag (Beaugé, Aarseth & Ferraz-Mello 1994), and, in the case of diffuse planetary rings, electromagnetic effects as well (e.g. Burns 1984).

* E-mail: richards@cita.utoronto.ca

A new code for simulating planetesimal dynamics was presented in an earlier paper (Richardson 1993, hereafter Paper I). The code (called `box_tree`) was developed with Solar system formation in mind, but in fact was derived largely from a method of local planetary ring simulations by Wisdom & Tremaine (1988, hereafter WT). The code incorporates a fourth-order force polynomial integration algorithm with individual time-steps (Aarseth 1985) and a full hierarchical tree code (e.g. Barnes & Hut 1986) to deal with gravitational interactions between particles.

The motivation for using numerical methods to study planetary rings (notably the rings of Saturn) stems from the inherent complexity of such systems. Analytical treatments (e.g. Goldreich & Tremaine 1978) have been limited to systems of identical non-self-gravitating particles and are necessarily only crude approximations of the true behaviour, providing a very coarse picture of the dynamical evolution of the rings. Local planetary ring simulations were developed as a first step towards numerically modelling the fine irregular structure of Saturn's rings. Unsolved problems include understanding the azimuthal asymmetry seen in Saturn's A ring and the

strong optical depth variations seen in the B ring, structure that is not attributed to resonances with known satellites. Possible explanations include viscous instability, liquid-solid phase transitions, or unstable density waves (see WT for a short review). Recent work (discussed below) suggests that formation of aggregate particles may play an important role. The latest numerical codes are on the verge of being able to differentiate between these possibilities.

In this paper, the original planetary ring problem as formulated by WT is reconsidered with the aid of `box_tree`. The new code allows the introduction of full self-gravity, a general particle size distribution, and surface (tangential) friction giving rise to particle spin, but with a speed advantage provided by the tree code to make realistic simulations practical in a workstation environment. Most of the analysis performed by WT will be applied to the new models, with appropriate modifications. It will be shown that the stratification seen in the mean self-gravity model still develops with equal-size self-gravitating particles, but evolves into complex three-dimensional aggregation when a realistic size distribution is introduced. It will also be shown that the condition for viscous instability is not satisfied in any of the models tested.

Recent work by Salo (1991, 1992a,b) has been directed at adding similar refinements of self-gravity and size distributions to the WT scheme. In particular, Salo (1992b) reports on the formation of gravitational wakes in Saturn's A and B rings using a low optical depth model, a find that is confirmed for the B ring in this paper. Salo shows that metre-sized aggregates form in the wakes and suggests that these may explain some of the non-uniformities seen in Saturn's outer rings. Salo uses vectorized code on an IBM mainframe ($\gtrsim$10 Mflops), but employs a less sophisticated integration algorithm with constant time-steps (Salo, private communication), which may limit accuracy in higher optical depth regimes. A proper study of the aggregates will probably require the improved accuracy of the code presented here in order to treat particle interactions in the clumps in a self-consistent manner. It is hoped that the current study will complement Salo's work and provide new insights into the planetary ring problem.

The numerical method is described in detail in Section 2, with particular emphasis on the changes that have been made to `box_tree` for the current project. First, however, a short summary of the original `box_tree` code and the WT method is presented (Section 2.1). The equilibrium properties of the simulation models are given in Section 3, beginning with a description of the common parameters. A comparison with WT's results is given in Section 3.2, while new results are discussed in the remaining subsections. A summary and further comments are presented in Section 4.

2 NUMERICAL METHOD

In what follows, a basic familiarity with the work of WT is assumed. A brief summary of the `box_tree` code is given first, but the reader is referred to Paper I for a fuller presentation. Extensions and modifications to the code needed to incorporate initial mass distributions and to improve collision treatment for the self-gravity case are discussed in detail in the remaining subsections.

2.1 Summary of '`box_tree`' and the WT method

The `box_tree` code is built on the premise employed by WT that a dense planetary ring can be divided into self-similar patches orbiting the planet, where the patch or box size L is larger than the radial mean excursion of the constituent particles but much smaller than the orbital distance. A convenient coordinate system to use is one centred on the box, with the x-axis pointing radially outward from the planet, the y-axis pointing in the direction of motion, and the z-axis pointing out of the orbital plane according to the right-hand rule. Under these conditions it is possible to linearize the equations of motion:

$$\begin{aligned} \ddot{x} &= \mathscr{F}_x + 3\Omega^2 x + 2\Omega\dot{y}, \\ \ddot{y} &= \mathscr{F}_y - 2\Omega\dot{x}, \\ \ddot{z} &= \mathscr{F}_z - \Omega^2 z, \end{aligned} \tag{1}$$

where $\boldsymbol{\mathscr{F}} = (\mathscr{F}_x, \mathscr{F}_y, \mathscr{F}_z)$ is the gravitational force per unit mass due to the ring particles and $\boldsymbol{\Omega} = \Omega\hat{\boldsymbol{z}}$ is the angular velocity of the box centre about the planet.

In order to provide realistic boundary conditions, the 'central' box is surrounded by eight ghost boxes in the orbital plane, each containing images of the central particles with the same relative positions. The number of particles N in the central box remains constant with time (merging is disabled for these simulations); particles leaving the central box are replaced with their appropriate ghost images entering from one of the surrounding boxes. The boxes with $x = \pm L$ experience shear with respect to the central box, complicating the boundary conditions.

A tree code (cf. Barnes & Hut 1986) is incorporated into `box_tree` for fast calculation of inter-particle gravitational forces. It is convenient to use a two-dimensional (2D) tree fitted over the central box since the disc system is relatively flat. Speed and accuracy are controlled by the opening-angle parameter θ_C: larger values permit shorter calculation times but give less accuracy. For the simulations discussed here, θ_C was fixed at 0.6 rad, offering considerable speed-up while introducing a mean error in the force calculations of less than 1 per cent (cf. Paper I). The speed increase is achieved by performing multipole expansions of the gravitational force over cells of dimension smaller than the distance times θ_C, rather than summing over each of the individual particles. In general, the CPU time increases as $\mathcal{O}(N \log N)$ when using the tree code, as compared with $\mathcal{O}(N^2)$ for a traditional direct method. Because of the unique geometry of the flattened disc system, the coefficient in front of the tree code scaling law is not as large as for traditional systems (e.g. Hernquist 1987), so that the tree becomes beneficial for N as small as 25 central particles (225 total). For a given value of N, however, the CPU expense may increase rapidly with optical depth (density), depending on the model used (see Section 3). A typical self-gravity run with $N = 50$ equal-sized particles and $\tau \gtrsim 2.5$ takes between 12 and 24 CPU hours to complete 30 orbits on a Sparc IPX (on the order of 10^6 collisions), about a factor of 2 faster than a direct method. Faster CPU times could be achieved, but it was decided that accuracy (particularly with regard to collision detection) was a more important consideration for this project. See Paper I for a detailed description of the modifications made to the traditional tree code for the planetesimal problem.

Particle predictions are carried out using a fourth-order polynomial integration algorithm with individual time-steps

based on a technique given by Aarseth (1985). It should be stressed that this algorithm was used even for those models that did not incorporate self-gravity (inter-particle gravitational forces). In WT, advancement proceeded from collision to collision using an iterative search, since equation (1) can be solved exactly for the homogeneous case $\mathscr{F} \equiv 0$; in `box_tree`, there is no prior knowledge of collision events.

2.1.1 *The WT method*

The basic technique used by WT for local simulations of planetary rings is to fill the central box with a representative population of particles in a configuration that is not at equilibrium, and then to allow the system to evolve to a stable configuration. The final state consists of a balance between energy dissipation from collisions and excitation by gravitational pumping, largely determined by the coefficient of restitution (Goldreich & Tremaine 1978). A number of simulations at different dynamical optical depths τ were performed by WT, for three different models of restitution coefficient and mean self-gravity (see Section 3.1 for details). The `box_tree` code has been modified to allow easy reproduction of the WT experiments, as well as extension beyond their simulations.

An attempt was made to conform as much as possible to the initial conditions and analysis method used in WT. In particular: box sizes were fixed by the number of particles and the desired optical depth (cf. Section 2.2.1); initial particle positions were chosen randomly within the box, with a uniform distribution in z up to a pre-set distance above and below the plane; particles were placed in pairs symmetrically (mass-weighted in the case of non-uniform sizes; see Section 2.2) to make the centre of mass coincide with the origin; particle velocities were chosen randomly in each coordinate with a uniform distribution up to Ω times the maximum particle radius, with the velocity of the last particle being set so that the centre-of-mass velocity was zero. Most runs consisted of 30 orbits of 50 central particles (slightly more particles than were used in WT). Collection of statistics was performed at fixed intervals, typically every tenth of an orbit. Quantities measured included the CPU time, the number of collisions, the velocity dispersion in each coordinate, the filling factor at the midplane ($z = 0$), the mean free path, the local viscosity, and the vertical particle distribution. Non-local viscosity data were collected for every tenth collision. Equilibrium properties were determined by estimating the onset of equilibrium from a plot of the number of collisions per particle per orbit, and averaging the desired quantities over the equilibrium interval. Errors reported are the standard deviation of the mean. It was found that a simple estimate of equilibrium onset is sufficient; a precise determination makes little difference to the results. Note that the WT technique of inhibiting the 'sliding phase' – where two or more particles come to rest and begin to roll around one another (cf. Petit & Hénon 1987) – was also incorporated into `box_tree`.

2.2 Initial mass function

The initial mass function (IMF) used to generate particle masses is derived from

$$n(m) \propto m^{\alpha},$$

where $n(m)\mathrm{d}m$ is the number of objects with mass in the range $[m, m + \mathrm{d}m]$, and α is a dimensionless parameter. Let $N(m)$ be the cumulative distribution, such that $\mathrm{d}N/\mathrm{d}m = n(m)$. Integration between $m_{\min}$ and m gives

$$N(m) = \frac{m_{\min}^{\alpha+1}}{\alpha+1}\left[\left(\frac{m}{m_{\min}}\right)^{\alpha+1} - 1\right], \quad \alpha \neq -1.$$

The total number of particles N is simply $N(m_{\max})$. Let $f = N(m)/N$ and solve for m:

$$m = m_{\min}\left\{1 + f\left[\left(\frac{m_{\max}}{m_{\min}}\right)^{\alpha+1} - 1\right]\right\}^{\frac{1}{\alpha+1}}. \tag{2}$$

This equation is equivalent to

$$m = \left[(1-f)m_{\min}^{\alpha+1} + f m_{\max}^{\alpha+1}\right]^{\frac{1}{\alpha+1}},$$

which is less computationally efficient but somewhat more intuitive. Masses are chosen by replacing f with uniform deviates between 0 and 1, or, for a smooth distribution, with values varied monotonically from 0 to 1 in steps of N^{-1}.

To obtain a size (radius) distribution in place of a mass distribution, write

$$\mathrm{d}N \propto R^{\alpha^*}\mathrm{d}R.$$

Assuming constant particle density ($m \propto R^3$), a substitution of variables gives

$$\mathrm{d}N \propto m^{\frac{\alpha^*-2}{3}}\mathrm{d}m.$$

Hence the correct size distribution can be obtained by setting

$$\alpha = \frac{\alpha^* - 2}{3} \tag{3}$$

in equation (2).

For large N, global properties of the mass distribution (e.g. total mass, mean mass, mean radius, etc.) can be well approximated by integrating appropriate powers of m in equation (2). For example, the mean mass can be estimated by setting $f = x/N$ and integrating the IMF in the range $[0, N]$ in x to give

$$\overline{m} \approx \left(\frac{\alpha+1}{\alpha+2}\right)\left(\frac{m_{\max}^{\alpha+2} - m_{\min}^{\alpha+2}}{m_{\max}^{\alpha+1} - m_{\min}^{\alpha+1}}\right), \quad \alpha \neq -1, -2.$$

For N as low as 50, this estimate is still good to about 10 per cent.

Values of $m_{\min}$ ($R_{\min}$), $m_{\max}$ ($R_{\max}$), and α (α^*) used in the simulations are given in Section 3.1.

2.2.1 *New definitions*

Non-uniform particle sizes complicate the definitions of some of the basic model parameters. For example, the box size in each simulation is determined by the dynamical optical depth τ. For non-uniform particle sizes, τ is defined by

$$\tau \equiv \frac{\sum_{i=1}^{N} \pi R_i^2}{L^2}. \tag{4}$$

If necessary, the sum in equation (4) can be estimated using the technique described above.

New expressions for the local and non-local viscosities must also be derived for the case of non-uniform particle sizes. Using the notation of WT, the local viscosity is given by

$$\bar{\nu}_{\rm L} = \frac{3}{2\Omega} \frac{< \sum_i m_i \dot{x}_i \dot{y}_{{\rm r},i} >_t}{\sum_i m_i}, \tag{5}$$

where $\dot{x}_i$ is the radial speed of particle i, $\dot{y}_{{\rm r},i} \equiv \dot{y}_i + \frac{1}{2}\Omega x_i$ is the tangential speed relative to the mean shear at x_i, and $<\cdot>_t$ denotes a time average measured from the onset of equilibrium to the end of the run. The non-local viscosity, which arises from collisional transport of angular momentum, is given by

$$\bar{\nu}_{\rm NL} = \frac{3}{2\Omega} \frac{1}{N\Delta T} \frac{\sum m_> (x_> - x_<) \Delta \dot{y}_>}{\bar{m}_>}, \tag{6}$$

where the subscripts '<' and '>' denote particles with $x < x_0$ and $x > x_0$, respectively, where x_0 is the radial coordinate of the impact point (that is, the surface contact point between the two particles), $\Delta \dot{y}_>$ is the change in y velocity of the particle with $x > x_0$, and the sum is over all collisions between the onset of equilibrium and the end of the run, a total time ΔT.

2.3 Collision detection

The two-body collision detection algorithm outlined in Paper I proved inadequate for some of the simulations discussed here, particularly in self-gravity models at high optical depth ($\tau \gtrsim 2$). As mentioned in Paper I, collisions are detected *after* they have actually occurred; that is, two particles are said to have collided if the sum of the colliders' radii exceeds the separation of their centres. The goal is to minimize the penetration distance prior to detection. Under the severe conditions of the planetary ring problem, where high optical depths give rise to large collision frequencies and a mean free path smaller than the mean particle size, the penetration distance can be quite large using the previous method ($\sim$ 50 per cent). The new technique, which entirely replaces the old one, can be divided into four distinct parts: (1) a time-step based on the distance between sphere *surfaces* rather than centres and the introduction of a more sensitive time-step formula for self-gravity models; (2) an improved collision prediction procedure; (3) position corrections after a collision has been established; and (4) a check for 'missed' collisions. These aspects will be discussed in more detail below.

2.3.1 *New time-step formulae*

If inter-particle gravity is not treated in the simulation (as for the WT models), the following formula is used to calculate the optimal time-step of a particle given the position and velocity of its nearest *approaching* neighbour:

$$\delta t = \eta \left[\frac{r - \varepsilon(R_1 + R_2)}{v} \right], \tag{7}$$

where η is the dimensionless time-step coefficient, r is the magnitude of the relative position $\boldsymbol{r} = \boldsymbol{r}_2 - \boldsymbol{r}_1$ measured between the centres of the particle and its neighbour, $R_1 + R_2$ is the sum of the particle radii, and v is the magnitude of the relative velocity $\boldsymbol{v} = \boldsymbol{v}_2 - \boldsymbol{v}_1$. An approaching neighbour is defined as one for which $\boldsymbol{r} \cdot \boldsymbol{v} < 0$ (particle trajectories are generally well-behaved when there is no inter-particle gravity, so approaching neighbours are the most likely colliders). The parameter ε determines what fraction of the finite size of the particles is included. If $\varepsilon = 0$, the sizes are ignored and the equation reduces to the traditional time-step formula. If $\varepsilon = 1$, the 'true' particle separation is used, measured from surface to surface along the line connecting the particle centres. Since the latter case can result in very short time-steps, the computation time may increase significantly when there are many close encounters and collisions. The CPU dependence turns out to be more or less exponential with ε. In fact, $\varepsilon = 0.99$ is typically twice as fast as $\varepsilon = 1$ but still gives very good accuracy, so this value was adopted for the original WT mean self-gravity model. The ε adjustment was not required for the other WT models.

Equation (7) is inadequate for 'true' self-gravity models. Consider, for example, a very close encounter in which the particle trajectories undergo considerable distortion. The above formula may give good results during the approach, but immediately after the encounter the second particle will be ignored in favour of a different approaching particle when determining the new time-step. This neglects the strong gravitational effects that will still be present after closest approach. Hence, for the self-gravity case, the $\boldsymbol{r} \cdot \boldsymbol{v} < 0$ criterion is no longer safe. Further, the time-steps will generally be too large immediately following a collision, since the quantity $\boldsymbol{r} \cdot \boldsymbol{v}$ may change sign in just a few time-steps due to the mutual gravitational attraction. In short, the time derivatives of the total force acting on a particle must be taken into account when choosing a time-step to allow for complicated interactions with close neighbours. A simple formula is

$$\delta t = \eta \frac{\mathscr{F}}{\dot{\mathscr{F}}},$$

where $\mathscr{F}$ is the magnitude of the force per unit mass. This breaks down, however, under certain symmetric conditions, and is not sufficiently sensitive at very small separations, especially in a strong tidal field. A more robust version, used by Aarseth (1985), is

$$\delta t = \sqrt{\eta \frac{\mathscr{F}\ddot{\mathscr{F}} + \dot{\mathscr{F}}^2}{\dot{\mathscr{F}}\dddot{\mathscr{F}} + \ddot{\mathscr{F}}^2}}. \tag{8}$$

Note that information regarding the closest neighbour is only implicit in this formula, contributing the larger part of the force derivatives. Identification of the closest neighbour is only used for collision determination (Section 2.3.2). This formula is expensive to compute, especially if `box_tree` first needs to convert from divided differences to the Taylor series terms (which is usually the case), but the benefits gained from increased sensitivity far outweigh such considerations.

To save time, equation (7) could be used when the nearest neighbour is approaching and equation (8) when it is receding. However, since it is short-range interactions that are of crucial importance in these simulations, only equation (8) was used throughout the self-gravity models (with one exception – see Section 3.5). It should be noted that the time-step coefficients η in equations (7) and (8) need not be the same, but, in the form they are given here, η values in the range 0.005–0.05 generally give good results.

2.3.2 *Improved prediction procedure*

Potential colliders are identified as part of the force calculation procedure in order to minimize the number of predictions and distance measurements to be performed. Conveniently, the tree code automatically eliminates particles that are too far away to be likely colliders when it applies the opening-angle criterion

to its nodes (cf. Paper I). The closest particle (with $\boldsymbol{r} \cdot \boldsymbol{v} < 0$ if there is no self-gravity) is noted, along with its position and velocity predicted to first order and appropriately adjusted if the neighbour is a ghost. After the fourth-order semi-iteration correction to the current particle position and velocity, a check is made to see whether a collision may have occurred using the distance versus sum-of-radii criterion. If so, and if inter-particle gravity is included in the simulation, a check is made to ensure that the particles are indeed approaching one another, and are not left over from a previous collision.

If the pair satisfies these conditions, then a collision is probable. The position and velocity of the collider are predicted to high (third) order, adjusted for ghosts, and the sum-of-radii and $\boldsymbol{r} \cdot \boldsymbol{v}$ checks are repeated. If the particles are no longer found to be colliding, a 'near miss' message is generated and the collision is not recognized. Otherwise, a position correction is performed to adjust the particles so that they are just touching (Section 2.3.3), and $\boldsymbol{r} \cdot \boldsymbol{v}$ is checked for the last time. Though unlikely, it is possible that position correction prevents the particles from actually colliding. Otherwise `box_tree` proceeds to calculate the post-collision velocities.

Though tedious, these tests are needed to ensure correct behaviour under close-packed conditions.

2.3.3 *Position corrections*

Ideally, a collision should be detected the instant it occurs. Unfortunately, such precision is impractical so a certain amount of 'penetration' or temporary overlap is unavoidable. For low collision rates, errors introduced by such penetrations can be ignored, but when there are many collisions, especially between the same particles, two major problems arise: (1) angular momentum is not conserved because the collision equations (Section 2.4) assume the particles are just touching; and (2) self-gravitating particles may 'collide' again after their first bounce, *before they have completely separated*. The latter problem is potentially disastrous because under extreme conditions the particles involved will simply 'sink' into one another. A naïve solution to this problem would be to switch off the gravitational attraction between particles with $r < R_1 + R_2$, simulating a surface normal force. Unfortunately, a third particle could simply bounce into either of the first two before they drift apart, resulting in another sinking problem. Introduction of normal forces between *all* touching particles in an arbitrary aggregate, and inclusion perhaps of a restoring force at the surface to simulate 'stickiness' (see Watanabe (in preparation) for an example of sticky strings), is beyond the scope of the current project.

The most straightforward solution, which also addresses the problem of angular momentum conservation, is simply to displace the particles so that they are just touching before applying the collision equations. There are two ways of accomplishing this: (1) moving the particles outward along the line connecting their centres; or (2) tracing the particles back along their respective velocity vectors. The latter solution has the advantage, for small displacements, of reproducing the 'true' geometry just prior to the collision. However, to be consistent, the particles should really be advanced forward in time after resolving the collision, but this introduces far too many complications to be practical. Hence the post-collision positions and velocities will still be slightly inaccurate with this method. A more serious problem is that, for grazing collisions (which are quite frequent in a shearing disc), the displacements can become arbitrarily large and unrealistic.

The first method, displacing the colliders along the line connecting their centres, ensures a minimum displacement, namely half the penetration depth. Since the depth of penetration can be controlled somewhat by the choice of time-step coefficient (Section 2.3.1), this is a desirable property. The disadvantage is that the collision geometry is altered slightly, and it is possible (though unlikely) that the particles involved may no longer be colliding after the displacement. However, given the simplicity of the technique, and the fact that it effectively eliminates the sinking effect for self-gravitating particles, this method has been implemented in the code. In equation form, the particle offsets are given by

$$\boldsymbol{r}_1^{\mathrm{adj}} = \boldsymbol{r}_1 - \left(\frac{\Delta r}{r}\right)\boldsymbol{r}, \quad \boldsymbol{r}_2^{\mathrm{adj}} = \boldsymbol{r}_2 + \left(\frac{\Delta r}{r}\right)\boldsymbol{r},$$

where

$$\Delta r \equiv \frac{R_1 + R_2 - r}{2}.$$

A further refinement would be to weight the offsets according to particle mass, to minimize the effects of offsets on the larger particles. Note that $\varepsilon = 1$ (Section 2.3.1) can no longer be used with these corrections in place, as it would result in zero time-steps following collisions.

For completeness, a simple procedure for backtracking along particle velocity vectors is also given here. Write

$$\boldsymbol{r}_i^{\mathrm{adj}} = \boldsymbol{r}_i + \lambda_i \boldsymbol{v}_i \Delta t \quad (i = 1, 2),$$

where, to allow for particles moving in roughly the same or opposite directions,

$$\lambda_1 = \begin{cases} -1, & \boldsymbol{r} \cdot \boldsymbol{v}_1 < 0 \\ 1, & \boldsymbol{r} \cdot \boldsymbol{v}_1 > 0 \end{cases}, \quad \lambda_2 = \begin{cases} -1, & \boldsymbol{r} \cdot \boldsymbol{v}_2 > 0 \\ 1, & \boldsymbol{r} \cdot \boldsymbol{v}_2 < 0 \end{cases}.$$

To force the particles just to touch, set

$$(\boldsymbol{r}_2^{\mathrm{adj}} - \boldsymbol{r}_1^{\mathrm{adj}})^2 = (R_1 + R_2)^2.$$

Now solve the quadratic to obtain Δt, rejecting the root with the larger absolute value (both roots should be negative):

$$\Delta t = \frac{-\boldsymbol{r} \cdot \boldsymbol{v}^* \pm \sqrt{(\boldsymbol{r} \cdot \boldsymbol{v}^*)^2 - |\boldsymbol{v}^*|^2 \left[r^2 - (R_1 + R_2)^2\right]}}{|\boldsymbol{v}^*|^2},$$

where $\boldsymbol{v}^* \equiv k_2 \boldsymbol{v}_2 - k_1 \boldsymbol{v}_1$. This procedure is evidently more complicated than the first, but may be more suitable for isolated collisional systems that are not subjected to a strong tidal field.

2.3.4 *Missed collisions*

As explained in Paper I, particles that have just collided must be reinitialized; that is, their force polynomials must be recalculated. This is because the particle velocities (and hence any force derivatives containing velocity terms) have suffered a discontinuity as a result of the collision. Part of the reinitialization involves finding the closest neighbour and recalculating the time-step. Normally the closest neighbour would be the original collider, but at high optical depth it is quite possible for two or more particles to collide with and hence overlap the same particle during the same time-step. The position correction described in Section 2.3.3 can worsen the situation, by adjusting the current particle or its original collider into new

positions that overlap other particles. Under the new collision scheme, a check is made to see whether the new closest neighbour has indeed penetrated the current particle. If so, the current particle is assigned a very small step to ensure that it will be updated immediately, forcing collision resolution. In this way it is possible for many particles to bunch together tightly in a self-consistent manner. To do any better would probably require testing for multiple colliders at the outset, which for the current project would be an unnecessary added complication (especially since the assumption of spherical particles, for instance, is only an approximation).

For regimes with $\tau \lesssim 3.5$, it was found that setting of $\Delta t = 10^{-15}t$ as the new time-step worked quite well, where t is the current simulation time. A relative value is favoured over an absolute value, as the former is not subject to precision limitations. However, at very high optical depths ($3.5 \lesssim \tau \lesssim 4$), there is a danger of entering a nearly infinite loop in the form of a repeated series of position adjustments and missed collision corrections to the same particles (picture three particles in a straight line, all touching). To avoid this, more moderate values of Δt should be used, based on the time-step and update time of the missed collider. Thus, if a repeated series of corrections begins to take place, it will not be too long before another particle disturbs the cycle. A reasonable formula is

$$\Delta t = 0.01(t_0 + \delta t - t), \tag{9}$$

where t_0 and δt are the last update time and current time-step of the missed collider, respectively. The factor of 0.01 was determined empirically: the smaller the value, the closer the equation approaches the original formulation.

2.4 Collision resolution

Once a collision event has been firmly established, the post-collision velocities (both linear and angular) of the colliders must be determined. The following derivation is appropriate for rough spheres of arbitrary mass.

Consider two uniform colliding spheres with masses m_1 and m_2, radii R_1 and R_2, located at $\boldsymbol{r}_1$, $\boldsymbol{r}_2$ in a Cartesian space, with linear velocities $\boldsymbol{v}_1$, $\boldsymbol{v}_2$ and angular velocities (spins) $\boldsymbol{\omega}_1$, $\boldsymbol{\omega}_2$ (Fig. 1). Let $\boldsymbol{r} = \boldsymbol{r}_2 - \boldsymbol{r}_1$ and $\boldsymbol{v} = \boldsymbol{v}_2 - \boldsymbol{v}_1$ be the relative position and velocity of the spheres, respectively, and define a new coordinate system in the collision plane with orthogonal axes n (normal component) and t (transverse component). The normal component is directed along the line connecting the centres of the two spheres ($\hat{\boldsymbol{n}} \equiv \boldsymbol{r}/r$). Also define vectors connecting the sphere centres to the point of impact: $\boldsymbol{R}_1 = R_1\hat{\boldsymbol{n}}$, $\boldsymbol{R}_2 = -R_2\hat{\boldsymbol{n}}$. Hence define the (linear) spin velocities at the point of impact: $\boldsymbol{\sigma}_i = \boldsymbol{\omega}_i \times \boldsymbol{R}_i$, $i = 1, 2$. Let $\boldsymbol{\sigma} = \boldsymbol{\sigma}_2 - \boldsymbol{\sigma}_1$ be the relative spin velocity at the point of impact and $\boldsymbol{u} = \boldsymbol{v} + \boldsymbol{\sigma}$ be the total relative velocity. Lastly, let $M = m_1 + m_2$ be the total mass of the two-body system, and denote the moments of inertia of the spheres by I_1 and I_2, respectively ($I_i = \frac{2}{5}m_iR_i^2$ for uniform spheres).

2.4.1 *Governing equations*

In the following treatment, all post-collision quantities are denoted by primes ($'$). The linear impulse suffered by body 1 as a result of the collision is given by $m_1(\boldsymbol{v}_1' - \boldsymbol{v}_1)$. By Newton's Third Law, this must be the negative of the impulse suffered by body 2, hence

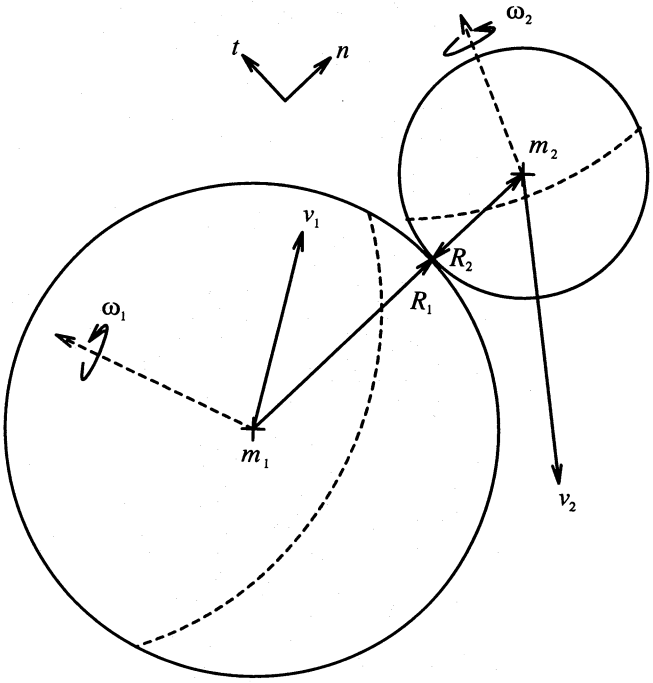

Figure 1. Diagram illustrating the basic collision definitions.

$$m_1(\boldsymbol{v}_1' - \boldsymbol{v}_1) = -m_2(\boldsymbol{v}_2' - \boldsymbol{v}_2). \tag{10}$$

By inspection, equation (10) is a statement of linear momentum conservation. The two spheres also suffer impulsive torques:

$$\begin{aligned} I_1(\boldsymbol{\omega}_1' - \boldsymbol{\omega}_1) &= m_1\boldsymbol{R}_1 \times (\boldsymbol{v}_1' - \boldsymbol{v}_1), \\ I_2(\boldsymbol{\omega}_2' - \boldsymbol{\omega}_2) &= m_2\boldsymbol{R}_2 \times (\boldsymbol{v}_2' - \boldsymbol{v}_2). \end{aligned} \tag{11}$$

It is straightforward to show that equations (10) and (11) together imply that angular momentum about the centre of mass of the two-body system is conserved. Finally, an expression for the energy loss resulting from the collision can be written as

$$\boldsymbol{u}' = -\epsilon_n\boldsymbol{u}_n + \epsilon_t\boldsymbol{u}_t, \tag{12}$$

where ϵ_n and ϵ_t are the normal and transverse coefficients of restitution, respectively, and $\boldsymbol{u}_n = (\boldsymbol{u} \cdot \hat{\boldsymbol{n}})\hat{\boldsymbol{n}}$ and $\boldsymbol{u}_t = \boldsymbol{u} - \boldsymbol{u}_n$ are the corresponding components of the total relative velocity.

2.4.2 *Post-collision velocities*

Solution of equations (10)–(12) for $\boldsymbol{v}_1'$ yields

$$\begin{aligned} \boldsymbol{v}_1' + \alpha\mu(\hat{\boldsymbol{n}} \times \boldsymbol{v}_1') \times \hat{\boldsymbol{n}} &= \boldsymbol{v}_1 + \alpha\mu(\hat{\boldsymbol{n}} \times \boldsymbol{v}_1) \times \hat{\boldsymbol{n}} \\ &+ \frac{m_2}{M}\left[(1+\epsilon_n)\boldsymbol{u}_n + (1-\epsilon_t)\boldsymbol{u}_t\right], \end{aligned} \tag{13}$$

where

$$\alpha \equiv \frac{R_1^2}{I_1} + \frac{R_2^2}{I_2}$$

and

$$\mu \equiv \frac{m_1m_2}{M}.$$

In the case of uniform spheres, $\alpha = \frac{5}{2}\mu^{-1}$. Solving by components and combining the results, the post-collision linear and angular velocities are given by

$$\boldsymbol{v}_1' = \boldsymbol{v}_1 + \frac{m_2}{M}\left[(1+\epsilon_n)\boldsymbol{u}_n + \beta(1-\epsilon_t)\boldsymbol{u}_t\right], \tag{14}$$

$$\boldsymbol{v}_2' = \boldsymbol{v}_2 - \frac{m_1}{M}[(1+\epsilon_n)\boldsymbol{u}_n + \beta(1-\epsilon_t)\boldsymbol{u}_t], \quad (15)$$

$$\boldsymbol{\omega}_1' = \boldsymbol{\omega}_1 + \beta\frac{\mu}{I_1}(1-\epsilon_t)(\boldsymbol{R}_1 \times \boldsymbol{u}), \quad (16)$$

$$\boldsymbol{\omega}_2' = \boldsymbol{\omega}_2 - \beta\frac{\mu}{I_2}(1-\epsilon_t)(\boldsymbol{R}_2 \times \boldsymbol{u}), \quad (17)$$

where

$$\beta \equiv \frac{1}{1+\alpha\mu}.$$

For uniform spheres, $\beta = \frac{2}{7}$. It can readily be shown that equations (14)–(17) reduce to equations (65-1)–(65-4) of Araki & Tremaine (1986) for the equal-mass case, though the results were derived independently.

A simple test was developed for checking the integrity of the collision code: seven equal-size randomly distributed inelastic spheres were started from rest in a plane (no particles touching) and allowed to interact. For reasonable values of η, the system quickly collapses and comes to rest at the system centre of mass in a symmetric configuration with negligible net linear and angular momentum, as required. This check has been incorporated as part of the standard `box_tree` test suite.

3 EQUILIBRIUM PROPERTIES

3.1 Model parameters

Six models were investigated for this paper, the first three reproducing the earlier WT results as a check, and the remainder exploring the new regimes of self-gravity, mass ranges, and particle spin. Initial conditions were as described in Section 2.1.1 for all models. Initial disc thicknesses varied, initially 10 particle radii but later 15 when problems developed in packing the box. Generally, initial disc thickness is not important so long as the initial configuration is not too close to equilibrium. Except for special cases investigated in the last model, the number of particles was kept fixed at $N = 50$, and integration was for 30 orbits. For the first five models, 20 values of dynamical optical depth τ were used, ranging from 0.2 to 4.0 in steps of 0.2 (WT studied $0.2 \leq \tau \leq 3.0$). A few τ values were chosen in each model for more detailed study. The models are

(i) velocity-dependent (normal) coefficient of restitution as obtained from experiment by Bridges et al. (1984): $\epsilon_n(v_n) = \min\left[0.34v_n^{-0.234}, 1\right]$, with v_n in cm s^{-1} (note that the factor of 0.34 is actually given as 0.32 in the original Bridges et al. paper);

(ii) velocity-independent restitution coefficient $\epsilon_n = 0.5$;

(iii) $\epsilon_n = 0.5$ as for model (ii) with mean self-gravity vertical frequency enhancement $g = 3.6$ such that $\ddot{z} = \mathscr{F}_z - g^2\Omega^2 z$ in equation (1);

(iv) velocity-dependent ϵ_n as for model (i) with full interparticle gravity using the tree code with $\theta_C = 0.6$ and monopole and quadrupole time-step coefficients of 0.001 and 0.01, respectively (cf. Paper I);

(v) velocity-dependent ϵ_n as for model (i), velocity-independent transverse restitution coefficient $\epsilon_t = 0.5$, full self-gravity, and a smooth size distribution (cf. Section 2.2) with $\alpha^* = -3$ ($\alpha = -\frac{5}{3}$). The exponent was chosen on the basis of observational data obtained by *Voyager* (Cuzzi et al. 1984). For this preliminary model, a conservative size range of 0.5–1 m was chosen (the observed range is ~1 cm–5 m for the R^{-3} power law);

(vi) as for model (v) but with several test cases for larger values of N and greater size ranges, including a comparison with work by Salo (1992b). Only a few values of τ were investigated, owing to the significant CPU expense of these models.

Particle radii of $R = 100$ cm and a transverse coefficient of restitution $\epsilon_t = 1.0$ were used for all models except models (v) and (vi). The density of water ice ($\rho = 1$ g cm^{-3}) was used for the particles in models (iv) and (v), and $\rho = 0.9$ g cm^{-3} was used for comparisons with Salo (1992b) in model (vi). Models (i), (ii), and (iii) had a time-step coefficient $\eta = 0.05$ in equation (7) (Section 2.3.1) while models (iv), (v), and (vi) used $\eta = 0.005$ in equation (8). Models (i) and (ii) had $\varepsilon = 0$ while model (iii) used $\varepsilon = 0.99$. Any other exceptions will be noted as appropriate.

3.1.1 *Units*

Units have been chosen so that $GM_S = 1$, where G is the gravitational constant and M_S is the mass of Saturn. Lengths are in units of the radius of the B ring measured from the planet centre ($R_B \sim 10^{10}$ cm). Times and speeds are measured relative to the orbital time and speed at R_B, where $\Omega_B = 1.95 \times 10^{-4}$ rad s^{-1}. Most quantities have been converted back to familiar units for presentation. Note that 1 g cm$^{-3} = \frac{5}{3}$ in the new units.

3.2 Models (i)–(iii): comparison with WT

Table 1 gives equilibrium z velocity dispersions (σ_z) for two dynamical optical depths in model (i) and two in model (ii). The fourth column lists the equilibrium values found by WT (these are the only numerical values available from the paper; most results were presented graphically). The agreement is excellent and demonstrates the stability of the technique. The errors in the WT data are consistently larger, presumably due to the fact that fewer particles and a shorter integration time were used.

Table 1. Some equilibrium values of σ_z for models (i) and (ii).

Model	τ	σ_z (cm/s)	WT σ_z (cm/s)
(i)	0.2	0.0454 ± 0.0004	0.0450 ± 0.0007
(i)	1.0	0.0294 ± 0.0002	0.0292 ± 0.0003
(ii)	1.0	0.0217 ± 0.0001	0.0218 ± 0.0003
(ii)	2.0	0.0187 ± 0.0001	0.0193 ± 0.0002

A vertical distribution histogram is given in Fig. 2 for model (i) with $\tau = 0.2$ (compare with fig. 3 of WT). The dashed curve is the analytical model of Goldreich & Tremaine (1978):

$$n(z) = n_{\max} \exp\left(-\frac{1}{2}g^2\Omega^2 z^2/\sigma_z^2\right), \quad (18)$$

which is a good approximation at low optical depth. It can be seen that `box_tree` reproduces the expected behaviour quite well.

Fig. 3 is a plot of the filling factor at the midplane FF(0) versus dynamical optical depth for models (i) and (ii). This should be compared with fig. 15 of WT. Note the change in

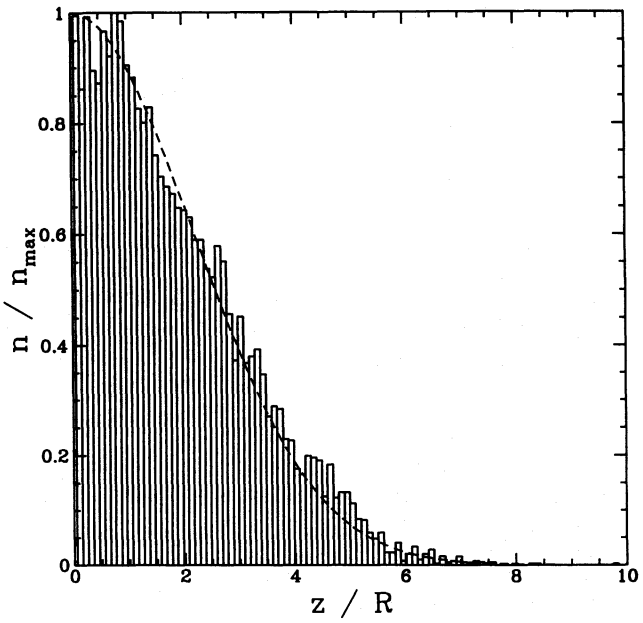

Figure 2. Histogram of the relative particle number density as a function of height above and below the $z = 0$ plane averaged over the equilibrium interval for model (i) with $\tau = 0.2$. The curve represents equation (18).

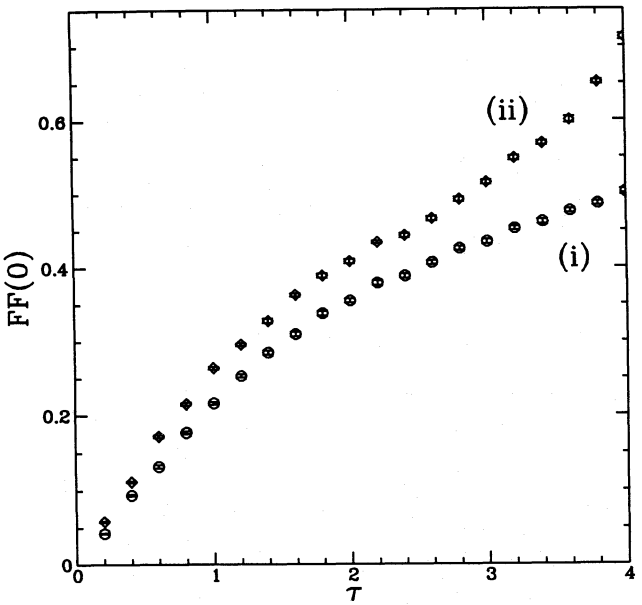

Figure 3. Filling factor at the midplane versus optical depth for models (i) (circles) and (ii) (diamonds). Note the turn-up in the model (ii) curve for $\tau > 2.5$.

behaviour of the two curves for $\tau \gtrsim 2.5$: the model (i) curve seems to have reached a constant slope while the model (ii) curve bends upward. This behaviour is suggested in the WT data, but the extended range in τ in Fig. 3 allows the effect to be seen more clearly. The behaviour can be understood by noting that the velocity-dependent coefficient of restitution makes collisions more elastic in model (i) as the velocity dispersion decreases, i.e. at higher optical depth. The filling factor still increases because the particles become more confined with optical depth, but the increase levels out as the collisions become more elastic. The constant coefficient of restitution in model (ii) allows the particles to bunch more strongly together with increasing τ, beyond the confinement effect.

Comparison with model (iii) begins with a plot of the Cartesian components of the velocity dispersion (Fig. 4). This plot in analogous to fig. 17 of WT. The dispersions are even more nearly equal in the `box_tree` run, emphasizing the fluid nature of the ring in this model. The splitting at $\tau \gtrsim 3.6$ is not understood. The most intriguing feature of the plot, however, is the strong downward spike near $\tau = 2.4$, which is not seen in the WT data. A corresponding feature is also seen in a plot of the filling factor (Fig. 5; compare with fig. 20 of WT). Blow-ups of the regions are shown in Figs 6(a) and (b). From the magnified plots, it would appear that some kind of critical point lies in the region $2.45 \lesssim \tau \lesssim 2.55$. Fig. 7 gives the vertical distribution for $\tau = 2.5$. The histogram shows that the system has developed almost perfect stratification, with three equally populated layers in the middle and two strongly underpopulated layers on the outside. This can be understood by noting that $N = 50$ and $\tau \approx 2.5$ give a box size of $L \approx 8R$ in equation (4). This would result in 4×4 packing on three levels, with two particles left over, presumably one either side. Note that, for close-packed sheets of spherical particles, the spheres on one level fill the gaps between spheres on neighbouring levels, hence the peaks in Fig. 7 do not occur at exact multiples of the particle size (except for the plane of particles at $z = 0$). Fig. 8 illustrates what close packing actually looks like as seen looking down on the shearing plane. It should be emphasized that such layering is probably unphysical as it depends on the ratio of the particle size to the (arbitrary) box size.

Other critical values of τ can be estimated by choosing positive integers n such that $L = 2nR$ and $n^2 \leq N$. For $N = 50$, there are 4 possible critical points in the range $0.2 \leq \tau \leq 4.0$, namely 2.45 (3 layers, 2 particles left over), 1.57 (2 layers, 0 left over), 1.09 (1 layer, 14 left over), and 0.80 (1 layer, 1 left over). The number density would be expected to vanish nearly at $z = 0$ for an even number of layers since the particles would straddle the midplane, rather than lie completely within it. This behaviour only partly explains the apparent oscillations in FF(0) for model (iii), however, because a local minimum occurs at $\tau \sim 1.3$, not $\tau = 1.57$ as might be expected (although a test was performed to confirm that $n(0)$ does indeed vanish for $\tau = 1.57$). A number density histogram for $\tau = 1.3$ shows the $z = 0$ level to be moderately populated (Fig. 9; compare with fig. 23 of WT). This discrepancy comes about because the overall increasing trend in FF(0) causes the critical values of τ to be shifted somewhat from their expected values.

3.3 Model (iv): Improved self-gravity model

The first step towards a more realistic planetary ring simulation is the inclusion of full particle self-gravity. As a test of the reliability of the force calculations, the full $0.2 \leq \tau \leq 4.0$ range was tested as before. Note that model (iv) lies somewhere between model (iii) and the zero-gravity case: the enhancement of the vertical frequency in model (iii) represented the contribution of the entire disc, whereas in model (iv) only the gravity of the central particles and their ghosts is included. Compensation for this could be made by increasing the particle density ρ, or introducing a smaller z frequency enhancement than was used in model (iii), but such detail was not considered impor-

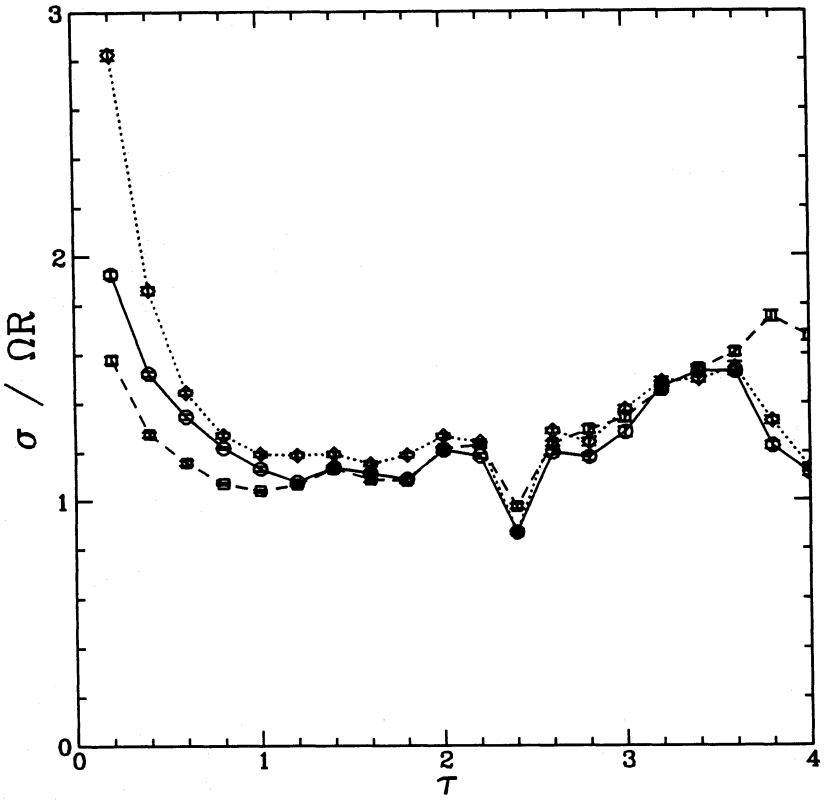

Figure 4. Cartesian components of the equilibrium velocity dispersion versus optical depth for model (iii). The x (radial) component is traced by diamonds (dotted line), y by squares (dashed line), and z by circles (solid line). Note the event near $\tau = 2.4$; this region is magnified in Fig. 6(a).

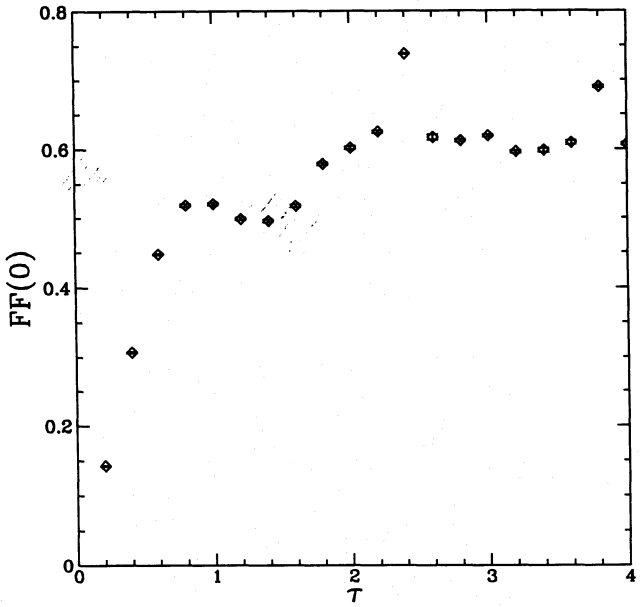

Figure 5. Filling factor at the midplane versus optical depth for model (iii). A blow-up of the region near $\tau = 2.4$ is shown in Fig. 6(b).

tant for these experiments. The particle number N was kept at 50: a plot of equilibrium velocity dispersion versus particle number was found to be essentially flat for $N \gtrsim 20$ (cf. fig. 1 of WT).

Fig. 10 shows the equilibrium velocity dispersions for model (iv) (compare with Fig. 4). Note that σ_z remains consistently smaller than σ_x and σ_y in this case. The blip near $\tau = 2.5$ still occurs, but with reduced significance. However, the filling factor (Fig. 11) shows that close packing still occurs to some extent in this model, though not as strongly. This behaviour is consistent with the reduced nature of the gravity enhancement compared with model (iii). The close packing is also noticeable in a plot of normalized $\tau\bar{v}$ versus τ (Fig. 12), where the slope goes negative in the region of $\tau = 2.5$, indicating a viscous instability associated with the (unphysical) close packing. With the exception of another unphysical point at $\tau = 4.0$, the slope of $\tau\bar{v}$ remains positive. Lastly, Fig. 13 shows the vertical distributions for 4 values of τ, clearly demonstrating that stratification persists in this model.

These models show that inclusion of particle self-gravity yields results that are similar to the mean self-gravity model. As will be shown below, however, full self-gravity becomes much more important once an initial size distribution is introduced into the system.

3.4 Model (v): size distribution model with rough spheres

Size distributions complicate the dynamics of numerical simulations considerably in the presence of self-gravity. As the system evolves, the largest particles gravitationally excite the smaller ones, making dynamic equilibrium harder to attain. The problem becomes more acute at low optical depth where there is little collisional dissipation. At higher optical depths, aggregates may form and further complicate the dynamics.

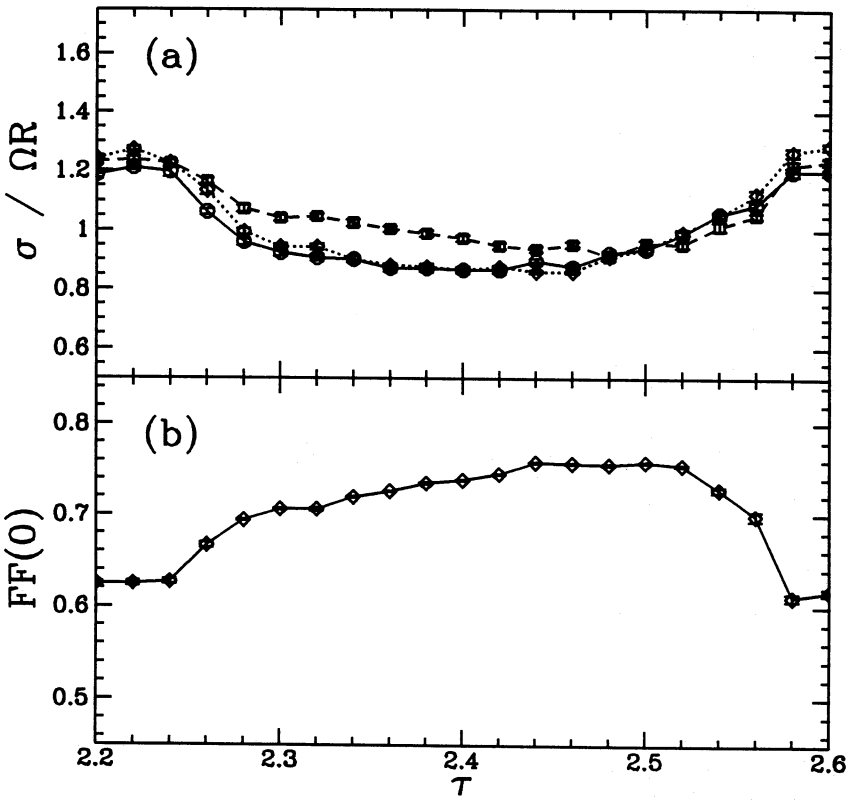

Figure 6. Blow-ups of the $2.2 \leq \tau \leq 2.6$ regions for the velocity dispersions (a) and filling factor (b) of model (iii). The transition is rapid but smooth.

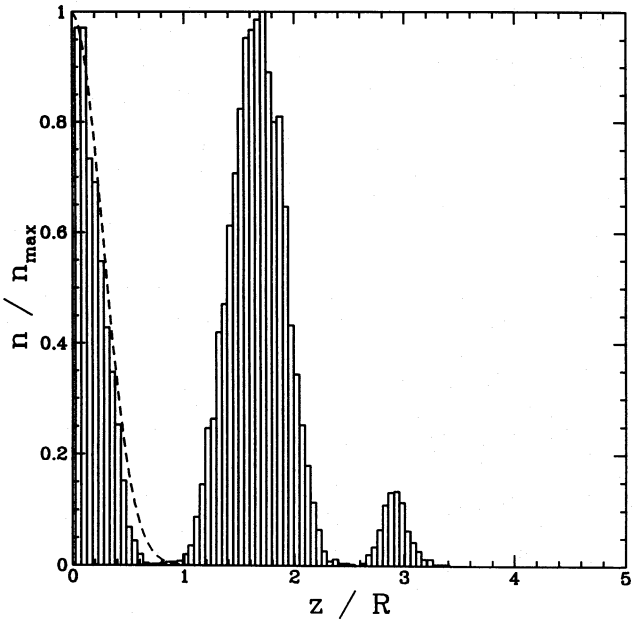

Figure 7. Vertical distribution of particles for model (iii) with $\tau = 2.5$. Five stratified layers have developed at this critical τ value.

Another problem is posed by the nature of the power-law distribution itself. As pointed out by Salo (1992a), N must be chosen large enough to provide statistically sound sampling of the size distribution. These aspects will be examined in greater detail in Section 3.5.

As a first test, and to provide a bridge between WT's simulations and later work by Salo, a series of runs in the spirit of model (iv) was performed for the conservative size range $\Delta R = 50$–100 cm. Although the size only varies by a factor of 2, the mass varies by a factor of 8, providing a good range of gravitational forces for this preliminary model. In addition, surface friction was incorporated in the form of a constant tangential coefficient of restitution, $\epsilon_t = 0.5$, in order to investigate the equilibrium distribution of particle spins. All spins were initially zero with respect to the local frame. The choice of $N = 50$ was checked in the usual way by verifying that the equilibrium velocity dispersion varied little for $N \in [10, 100]$ with $\tau = 1$; $N = 50$ also provides adequate sampling of the size distribution given the limited range.

Figs 14–16 show the usual statistical quantities for this model. The velocity dispersions (Fig. 14) behave much the same as for model (iv) (Fig. 10; note change in scale). The midplane filling factor (Fig. 15) is seen to attain and sustain a higher level, consistent with the improved packing efficiency of a size distribution. The curve is quite smooth with the exception of an unexplained blip at $\tau \sim 3.3$. The viscosity curve (Fig. 16) is very smooth and shows no evidence of viscous instability in the range $0.2 \leq \tau \leq 4$. Note that the size distribution effectively eliminates the 'crystallization' phenomenon found in models (iii) and (iv) for certain critical values of τ.

Figs 17–19 give the height, spin, and obliquity distributions for $\tau = 0.5$, 1.0, 2.0, and 3.0. The vertical distribution (Fig. 17) is similar to Fig. 13, though the dips are not as well defined and the mean height is smaller due to the tighter packing. The spin distribution (Fig. 18) evidently varies little

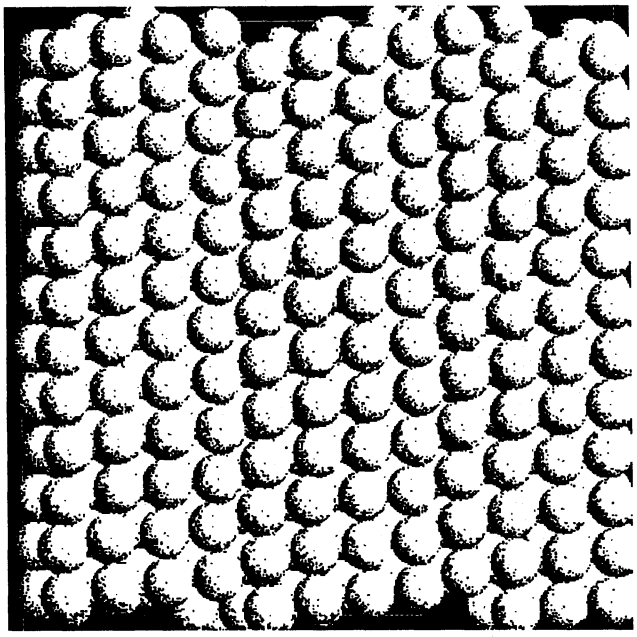

Figure 8. View looking down on to the ring plane for model (iii), $\tau = 2.5$, during the equilibrium phase. The central box plus all 8 ghost boxes are shown (450 particles in all, most hidden behind the top layer). At this critical τ value, several stratified sheets have formed, with particles lined up in y (bottom to top) to minimize resistance to the shearing flow.

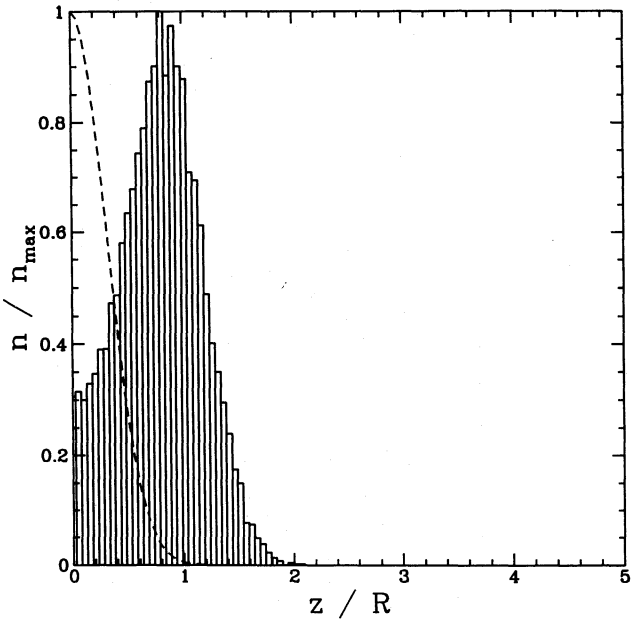

Figure 9. Number density histogram for model (iii) with $\tau = 1.3$. Though this value of τ gives a local minimum in FF(0) (cf. Fig. 5), the midplane is still moderately populated.

with optical depth. The dashed curve superimposed on each histogram is given by

$$n(\omega) = \omega e^{-\omega}. \tag{19}$$

This curve is drawn for reference only, without physical justification. Note that in all cases each particle has suffered at least one collision, so there are no zero spins remaining. The distribution in obliquity, or the angle ψ between the spin axis $\hat{\boldsymbol{\omega}}$ and the positive z-axis $\hat{\boldsymbol{z}}$ (Fig. 19), also varies little with optical depth, but shows a strong tendency toward retrograde spin ($\psi > 90°$). Recall that all spin properties are with respect to the local (rotating) frame of reference; in the fixed frame, the spins would be slightly prograde on average.

Further aspects of this model will be presented in the following section.

3.5 Model (vi): large-N models

In order to model a realistic size range at optical depths of order unity or higher in a statistically valid way, larger values of N must be used. Conversely, for a given value of N, the size range is constrained. For example, suppose a conservative box size $L = 10R_{max}$ is imposed. If $\tau = 1$ and $R_{max} = 5$ m, then R_{min} can be determined for a given value of N by integrating the equivalent of equation (2) in R. This gives

$$R_{min} \approx \frac{20}{\sqrt{N\eta_5}}, \tag{20}$$

where $\eta_5 \equiv \ln(5/R_{min})$ and sizes are measured in metres. Equation (20) can be solved iteratively for R_{min}. Models (vi.1–5) and (vi.7) were obtained by choosing $N = 200$, 400, 600, 800, 1000, and 3200, respectively, in equation (20). The results are summarized in Table 2. Also included in the table are the four runs $\tau = 0.5$, 1.0, 2.0, and 3.0 from model (v), labelled models (v.1–4). Model (vi.6) reproduces a run by Salo (1992b) and will be discussed in more detail below. The table shows the chosen equilibrium interval ΔT for each run, as well as the mean midplane filling factor (error bars omitted to conserve space). The mean z spin as seen from the fixed *inertial* frame μ^*, the mean spin magnitude and obliquity as seen in the local frame, the mean vertical distance from the plane, and the mean velocity magnitude are given for each run, split into three cases according to size bin. The quantity $\mu^* = \overline{\omega_z} + \Omega$ is included for comparison with Araki (1991), who found $\mu^* \sim 0.3$ for the equal-mass case. None of the quantities is mass-weighted since the binning automatically differentiates between the low- and high-mass regimes. It was found that five size bins gave adequate sampling (usually at least four particles in the largest bin): $\Delta R_b = \frac{1}{5}\Delta R$. The top line of each set is for $R_{min} \le R \le R_{min} + \Delta R_b$, the middle line is for the complete range $R_{min} \le R \le R_{max}$, and the bottom line is for $R_{max} - \Delta R_b \le R \le R_{max}$. The number of particles in each bin is listed in the column labelled N_b.

Note that the quantity μ^* varies between 0.15 and 0.45 when averaged over all particles in each model (omitting model (vi.7) for now), and there is a suggestion that the value decreases as the size range increases, possibly due to a stronger random contribution from the increasing number of smaller particles. This is supported by the fact that the mean z spin in the large particle bins is typically much larger than that for the small particle bins (recall that, at $t = 0$, $\omega_z = 0$ and so $\mu^* = 1$ for all particles initially). Evidently there is a preferred prograde spin of about 0.3 for the particles when viewed from the planet frame (for reference note that, in such a frame, Earth's Moon would have a prograde spin of unity). The other statistical quantities in the table will be discussed below within the contexts of models (v) and (vi).

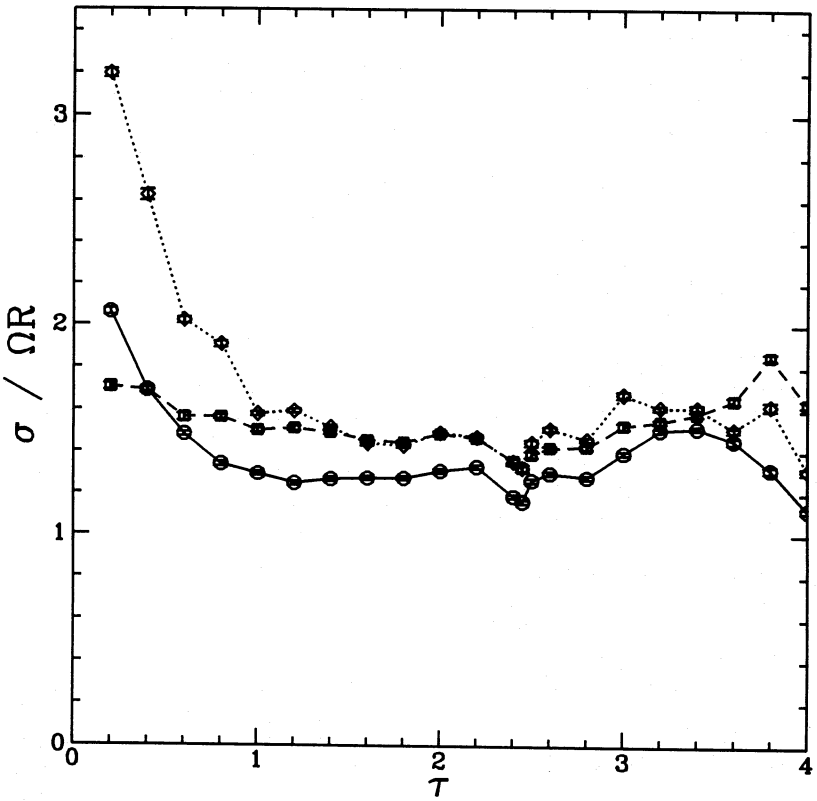

Figure 10. Equilibrium velocity dispersions for model (iv).

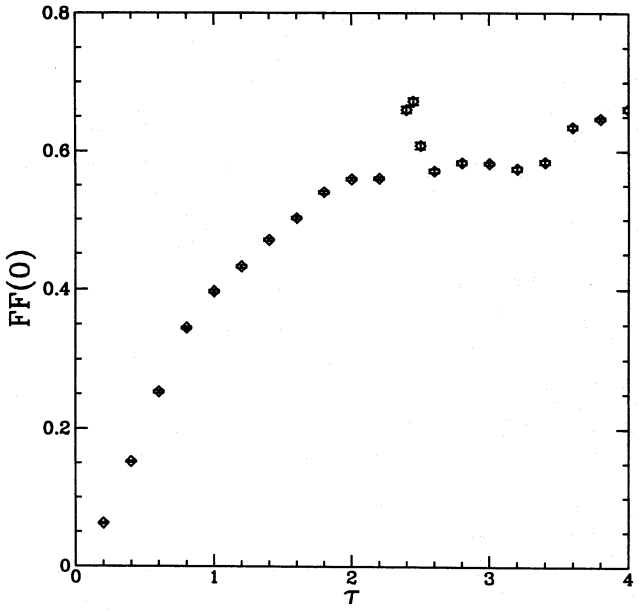

Figure 11. Midplane filling factor for model (iv).

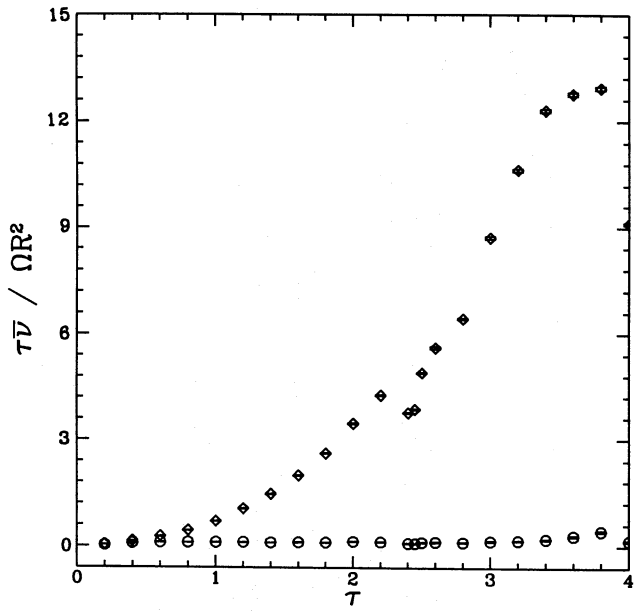

Figure 12. Dimensionless height-averaged kinematic viscosity times τ, versus τ. The local contribution (circles) is much smaller than the total contribution (diamonds) for moderate to large τ. The slope changes sign near the critical point $\tau \sim 2.5$, indicating a regime of viscous instability.

The data for models (v.1–4) confirm the trends shown in Figs 14–19. The data also show that the smallest particles have the largest spin, consistent with equipartition of rotational energy (this will be illustrated for model (vi.1) below). Interestingly, the smallest particles also have their mean spin axes most nearly orthogonal to the mean orbital axis, though the peak of the distribution is rather wide (Fig. 19). It should be noted, however, that, when the Cartesian components of the particles' spins are averaged *separately*, the x and y components turn out to have means $\ll \Omega$, leaving the spin in z dominant (i.e.

Table 2. Binned equilibrium data for models (v) and (vi).

Model	N	ΔR (m)	τ	ΔT (orb)	FF(0)	N_b	μ^* (Ω)	$\overline{\omega}$ (Ω)	$\overline{\psi}$ (°)	$\overline{\lvert z\rvert}$ (m)	$\overline{v}$ (cm/s)
						20	0.37	2.47 ± 0.01	105.9 ± 0.5	0.769 ± 0.007	0.0482 ± 0.0003
(v.1)	50	0.50–1.0	0.5	4–30	0.243	50	0.36	1.853 ± 0.008	113.8 ± 0.3	0.640 ± 0.004	0.0414 ± 0.0002
						4	0.32	0.98 ± 0.01	135 ± 1	0.373 ± 0.008	0.0298 ± 0.0004
						20	0.22	2.20 ± 0.01	110.7 ± 0.5	0.744 ± 0.005	0.0385 ± 0.0003
(v.2)	50	0.50–1.0	1.0	3–30	0.465	50	0.264	1.676 ± 0.007	118.7 ± 0.3	0.623 ± 0.002	0.0336 ± 0.0001
						4	0.36	0.87 ± 0.01	138.0 ± 0.9	0.389 ± 0.008	0.0245 ± 0.0003
						20	0.23	2.34 ± 0.01	108.8 ± 0.5	1.074 ± 0.007	0.0400 ± 0.0004
(v.3)	50	0.50–1.0	2.0	4–30	0.631	50	0.27	1.786 ± 0.007	116.1 ± 0.3	0.923 ± 0.002	0.0358 ± 0.0004
						4	0.36	0.92 ± 0.01	133.3 ± 0.9	0.54 ± 0.01	0.0291 ± 0.0005
						20	0.23	2.45 ± 0.02	108.2 ± 0.5	1.38 ± 0.01	0.0399 ± 0.0003
(v.4)	50	0.50–1.0	3.0	3–30	0.690	50	0.264	1.880 ± 0.008	115.4 ± 0.3	1.228 ± 0.003	0.0366 ± 0.0003
						4	0.29	0.99 ± 0.01	136.6 ± 0.9	0.82 ± 0.01	0.0306 ± 0.0004
						135	0.38	4.00 ± 0.02	99.9 ± 0.1	3.10 ± 0.01	0.2192 ± 0.0009
(vi.1)	200	1.15–5.0	1.0	3–10	0.373	200	0.432	3.22 ± 0.01	102.3 ± 0.1	2.96 ± 0.01	0.2124 ± 0.0009
						5	0.707	0.655 ± 0.006	116.8 ± 0.7	3.23 ± 0.03	0.236 ± 0.002
						326	0.19	7.39 ± 0.03	97.1 ± 0.1	4.84 ± 0.06	0.274 ± 0.001
(vi.2)	400	0.70–5.0	1.0	4–10	0.178	400	0.27	6.43 ± 0.02	97.8 ± 0.1	4.80 ± 0.06	0.269 ± 0.001
						4	0.43	1.17 ± 0.01	120.3 ± 0.5	6.25 ± 0.08	0.332 ± 0.003
						518	0.13	10.16 ± 0.03	95.60 ± 0.06	5.81 ± 0.08	0.313 ± 0.002
(vi.3)	600	0.55–5.0	1.0	3–10	0.145	600	0.20	9.13 ± 0.03	95.97 ± 0.07	5.77 ± 0.08	0.310 ± 0.002
						4	0.990	1.044 ± 0.006	88.6 ± 0.5	7.2 ± 0.1	0.368 ± 0.003
						715	0.18	12.39 ± 0.04	94.66 ± 0.08	4.13 ± 0.03	0.309 ± 0.002
(vi.4)	800	0.46–5.0	1.0	2–5	0.193	800	0.23	11.36 ± 0.04	94.99 ± 0.08	4.08 ± 0.03	0.305 ± 0.002
						4	0.86	1.217 ± 0.008	97 ± 1	7.0 ± 0.1	0.385 ± 0.004
						914	0.12	14.40 ± 0.08	94.17 ± 0.06	4.28 ± 0.04	0.302 ± 0.002
(vi.5)	1000	0.40–5.0	1.0	1–3	0.177	1000	0.16	13.40 ± 0.08	94.68 ± 0.07	4.23 ± 0.04	0.299 ± 0.002
						4	0.76	1.11 ± 0.02	102.9 ± 0.4	6.9 ± 0.1	0.376 ± 0.004
						2820	0.128	12.4 ± 0.1	94.98 ± 0.04	4.86 ± 0.04	0.341 ± 0.002
(vi.6)	3200	0.50–5.0	0.4	1–3	0.0854	3200	0.197	11.2 ± 0.1	95.27 ± 0.05	4.69 ± 0.04	0.335 ± 0.002
						16	0.979	0.76 ± 0.01	92.2 ± 0.2	5.80 ± 0.05	0.350 ± 0.003
						3109	−0.31	14 ± 2	58 ± 6	7.0 ± 0.5	0.27 ± 0.02
(vi.7)	3200	0.20–5.0	1.0	0–0.4	0.01	3200	−0.29	14 ± 2	59 ± 6	7.0 ± 0.5	0.27 ± 0.02
						3	0.71	0.49 ± 0.06	103 ± 5	7.1 ± 0.4	0.40 ± 0.03

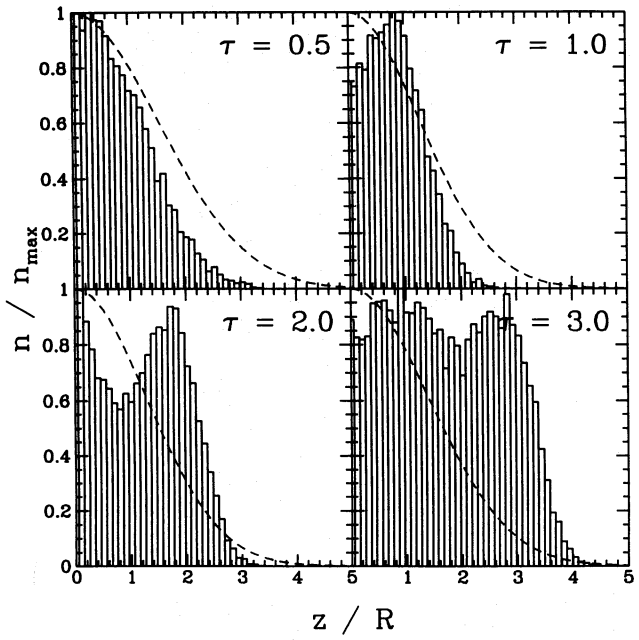

Figure 13. Number density versus $|z|$ histograms for model (iv) for τ = 0.5, 1.0, 2.0, and 3.0. Stratification is still seen in this model.

$\mu^* \sim 0.3$ as discussed above). This implies that the components of the spin vectors that lie in the orbital plane are isotropically distributed. As will be illustrated below, the mean component spins for all models have Lorentz profiles. Finally, note that the smallest particles have the largest z excursion and mean velocity, consistent with energy injection by gravitational scattering off the largest particles.

Models (vi.1–5) were studied for shorter intervals because of the increased CPU expense. This increase is due primarily to the scaling with N, but there is also an increase due to inhomogeneities in the particle distribution, namely the formation of cigar-shaped clumps or aggregates. These associations tend to pack quite tightly, increasing the force derivatives on the constituent particles and resulting in shorter time-steps according to equation (8). Fig. 20 illustrates one such aggregate. This snapshot of model (vi.4) was taken at $t = 3$ looking down the z-axis. Animations of the formation and evolution of these aggregates show several common features: (1) they have a characteristic *pitch angle* $\lambda \sim 30°$ measured with respect to the positive y-axis (the direction of mean orbital motion); (2) they tend to form around the largest particles; (3) they form and 'dissolve' within a few fractions of an orbit; (4) they are *not* seen when inter-particle gravity is switched off; (5) they do not form if the particles are equal-size (the model (v) runs,

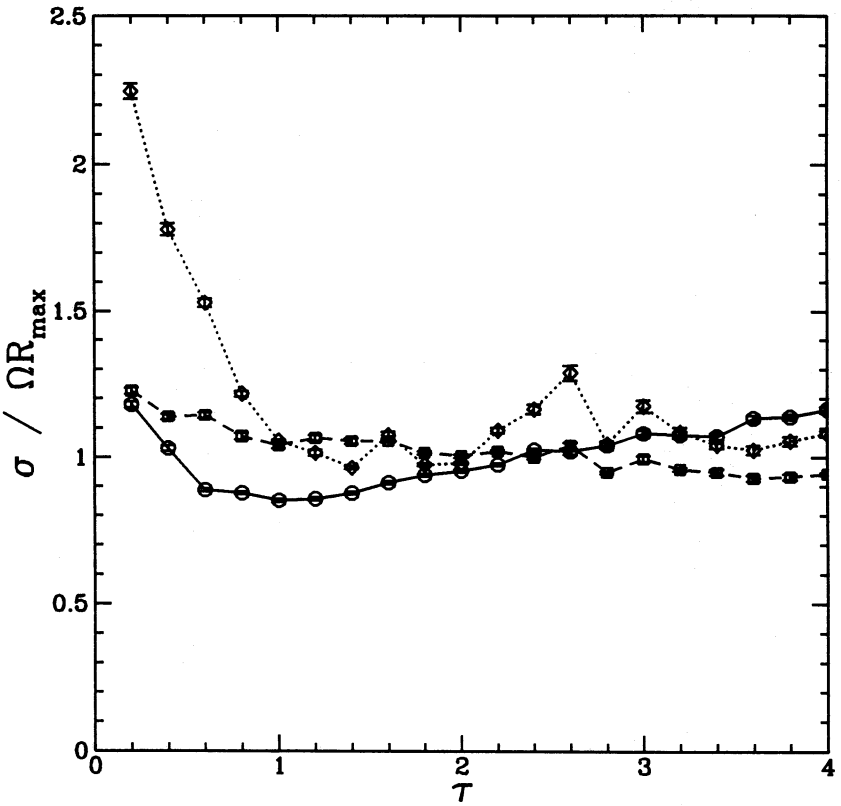

Figure 14. Equilibrium velocity dispersions for model (v).

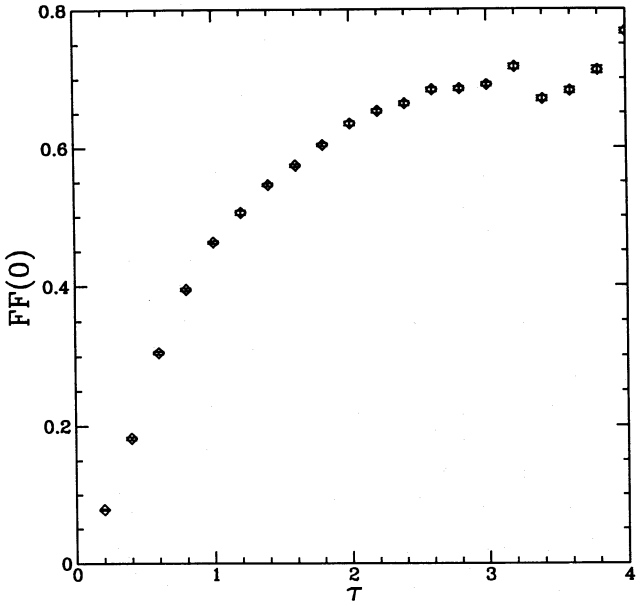

Figure 15. Midplane filling factor for model (v).

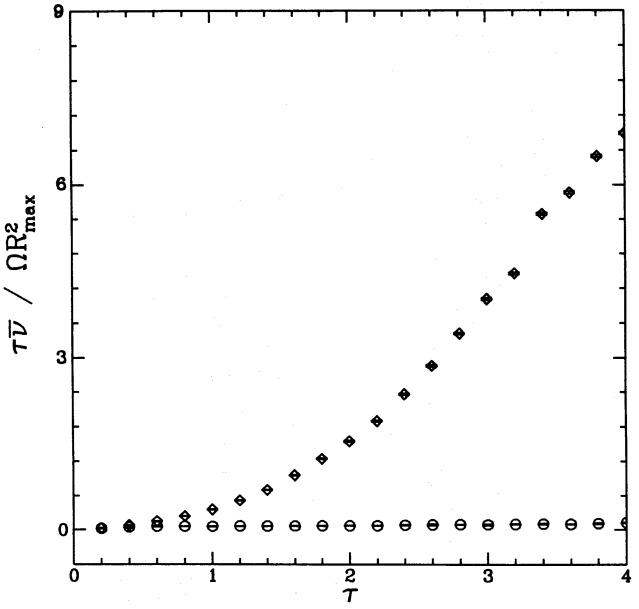

Figure 16. The quantity $\tau\bar{\nu}$ (normalized) versus ν for model (v). There is no evidence of viscous instability.

where the size range was small, developed loosely grouped associations). Aggregate formation will be discussed further below.

Particle aggregates help explain some of the anomalies seen in Table 2 for models (vi.1–5), namely the fact that the largest particles now seem to be dominant in the z excursion and mean velocity, contrary to the case of models (v.1–4). Evidently the aggregates behave like 'super-particles', trapping the smaller particles and reducing their contributions to the dispersions. The larger particles, meanwhile, are strongly perturbed by the clumps, so their contributions are increased.

The mean spin as a function of particle moment of inertia for model (vi.1) is shown in Fig. 21. The plot demonstrates

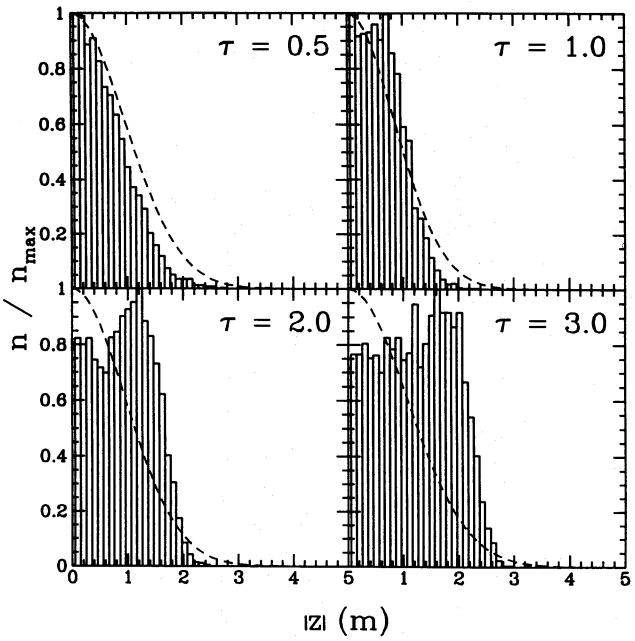

Figure 17. $n/n_{\max}$ versus $|z|$ for model (v) and four values of τ. The particles continue to pile up at high optical depth, but layering is not as well defined since smaller particles can start filling the gaps between larger particles.

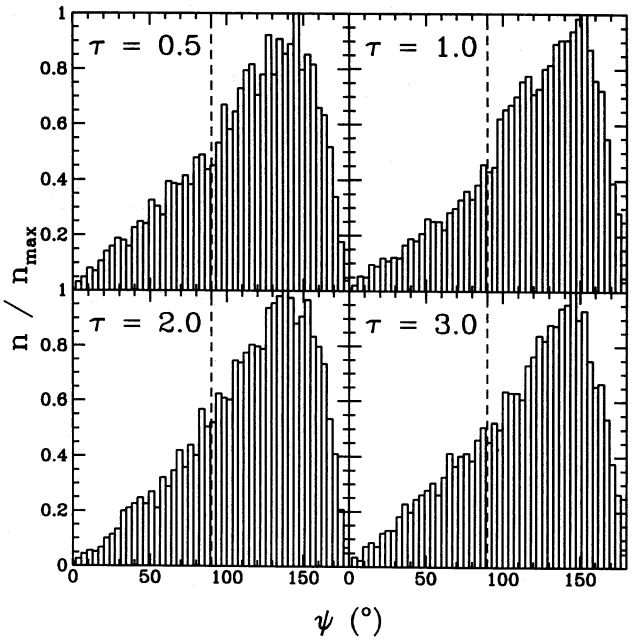

Figure 19. Relative number density as a function of spin obliquity (angle between spin and orbital momentum vectors) for model (v). Again there is little dependence on τ. The plots show that most particles are spinning retrograde with respect to their orbital motion when viewed from the rotating frame.

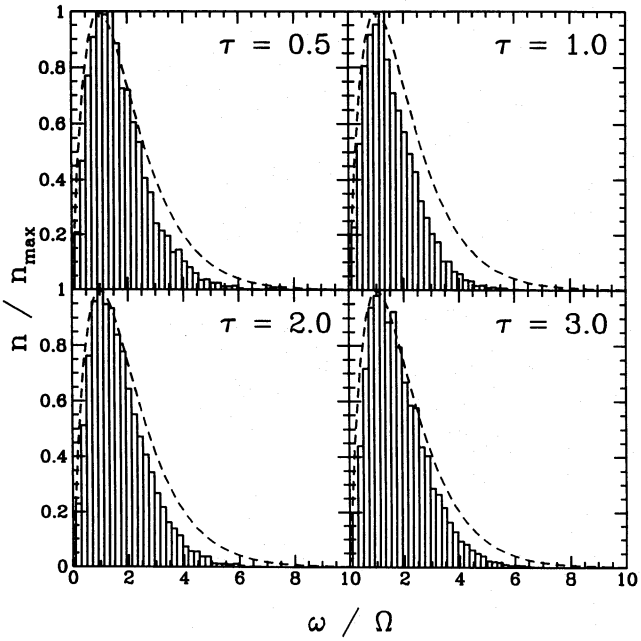

Figure 18. Relative number density as a function of spin magnitude ω (in units of Ω) for model (v). The dashed curve is given by equation (19). There is little dependence on optical depth for this model.

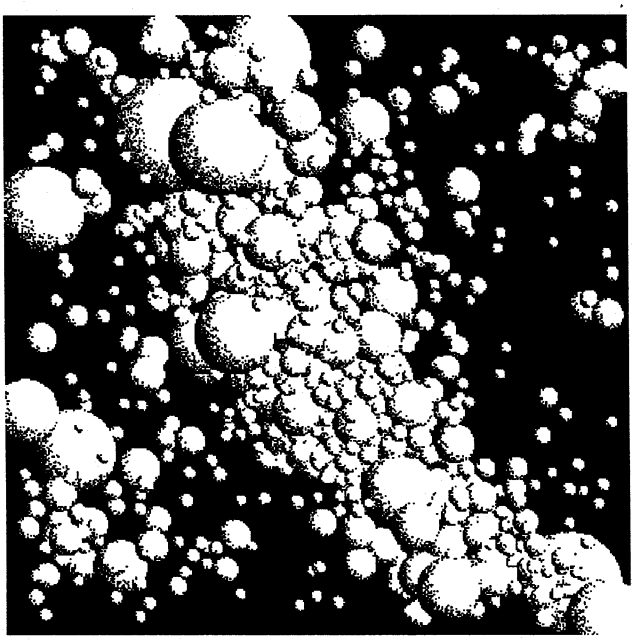

Figure 20. View of model (vi.4) at $t = 3$ looking along the negative z-axis. The box is 50 m on a side.

that, in the equilibrium state, rotational energy is distributed according to moment of inertia: smaller particles generally spin faster or have a greater range of spin energy. The dashed line shown in the plot is the isocurve $I\omega^2 = I_{\max}\Omega^2$, tracing an upper envelope to the spin distribution.

Model (vi.6) was designed to be a direct comparison with a recent result by Salo (1992b, fig. 1, B ring). The box size, dynamical optical depth, and size distribution were identical, as was the velocity-dependent (normal) coefficient of restitution. Tangential friction was included in model (vi.6), unlike the Salo model, but was not expected to affect the dynamics appreciably. The run was only carried out for 3 orbits owing to the CPU expense, but reached an acceptable equilibrium after 1 orbit. A combination of equations (7) and (8) was used for computing time-steps to improve the speed. Fig. 22 shows

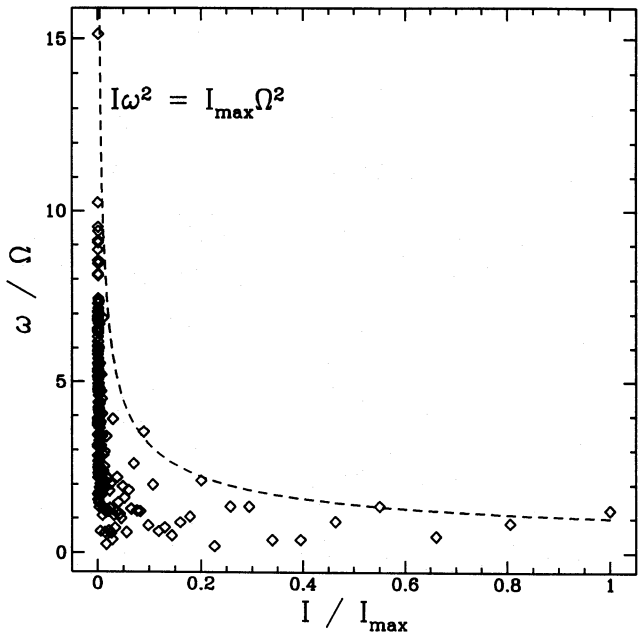

Figure 21. Mean spin as a function of moment of inertia for model (vi.1). The spins lie below an equipartition envelope $I\omega^2 = I_{\max}\Omega^2$.

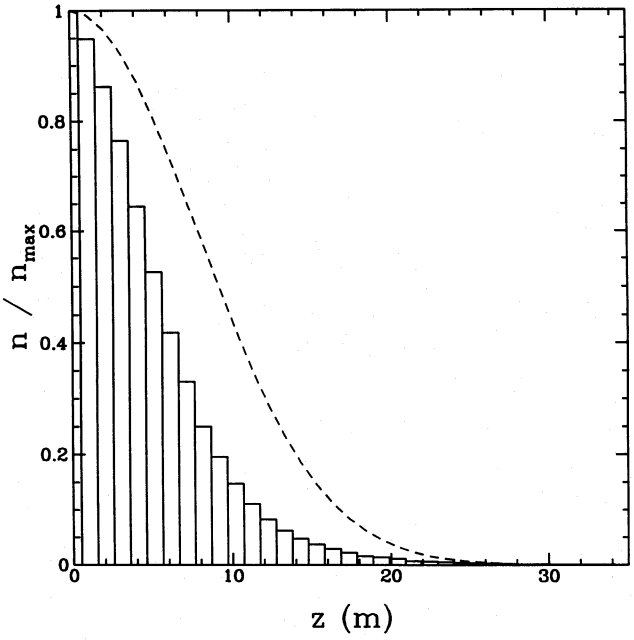

Figure 22. $n/n_{\max}$ versus $|z|$ for model (vi.6) after 3 orbits.

a very smooth vertical distribution, packed tighter than the curve given for the theoretical equal-size case without self-gravity. The spin distributions (all three components plus the spin magnitude) are shown in Fig. 23. Lorentzians of the form $1/(\omega_i^2 + 10)$ have been drawn for the ω_x, ω_y, and ω_z distributions as an aid to the eye. Similar Lorentz distributions in spin components occur for all models that include spin effects. The curve for the spin magnitude distribution is equation (19) with ω weighted by a factor of 0.2 to approximate the actual width of the distribution. The spin rates are much higher in this model, again dominated by the smaller particles. The spin obliquities are shown in Fig. 24. The obliquity distribution is very broad (FWHM $\sim 120°$), and only very slightly retrograde on average.

Fig. 25 shows snapshots at $t = 0$ and 3 (left and right), with views along the negative z-axis (top) and along the positive y-axis (bottom). The top right image should be compared with fig. 1 of Salo (1992b). The system has evidently developed the gravitational wakes or density transients reported by Salo, and predicted by Julian & Toomre (1966) for rotationally supported discs that undergo gravitational perturbation. The snapshot shows that aggregates are generally associated with these unstable waves. Indeed, the equilibrium state for model (vi) in general appears to be the continual formation and dissolution of such structures. Their orientation can be explained qualitatively by the differential rotation of the disc: any condensations that form suffer from shear in the $\pm y$-directions relative to their centres of mass, twisting and pulling the clumps into configurations that minimize the net differential force until other disruptive impacts occur. The observed pitch angle ($\sim 30°$) is consistent with values found by Salo (1992b) for three-dimensional simulations. Also note the evolution in z illustrated by the images at the bottom of Fig. 25: the system was started very flat (only a few $R_{\max}$) to encourage faster attainment of equilibrium; by $t = 3$ the system has relaxed into a typical equilibrium configuration.

The last model to be considered, model (vi.7), provides the most realistic simulation so far of conditions at the centre of Saturn's B ring, with a large size range $\Delta R = 0.2$–5 m and optical depth of unity. Unfortunately, because of the high density and large particle number, it is also the slowest to compute, taking several CPU days on a DEC Alpha workstation just to follow one complete orbit. Fig. 26 is a snapshot of the system at $t = 0.27$, already showing the formation of a transient density feature. The central box and surrounding ghost boxes are shown to emphasize the presence of the density enhancement. Though not yet at equilibrium, the statistical properties for this system given in Table 2 are consistent with trends seen in the other model (vi) runs (with the exception of the mean z spin: only ~ 60 per cent of particles have collided at this point).

An important trend seen in the table for the model (iv) runs with $\tau = 1$ is that the mean spin magnitude, z excursion, and velocity generally increase as the size range is extended, despite the fact that the runs all have the same dynamical optical depth. The apparent decrease in μ^* with increasing size range has already been mentioned. Together, these facts suggest that an accurate numerical determination of the equilibrium properties at the centre of Saturn's B ring *must* include the true size distribution. This means that even larger simulations are needed.

A disturbing aspect of some of the large-scale features reported here is that they can be comparable in size to the central box, and indeed may even extend beyond the box (see Fig. 26 for example). For a model that employs periodic boundary conditions, this means that such a structure may actually interact with itself, confusing the interpretation of the results. One possible consequence is that such structures break up and re-form more often in these models than they would in reality, or at least are truncated in size. Another related problem is that the mean velocities are fairly large in model (vi), implying large radial excursions (which are in fact seen in animations), possibly invalidating the local nature of the

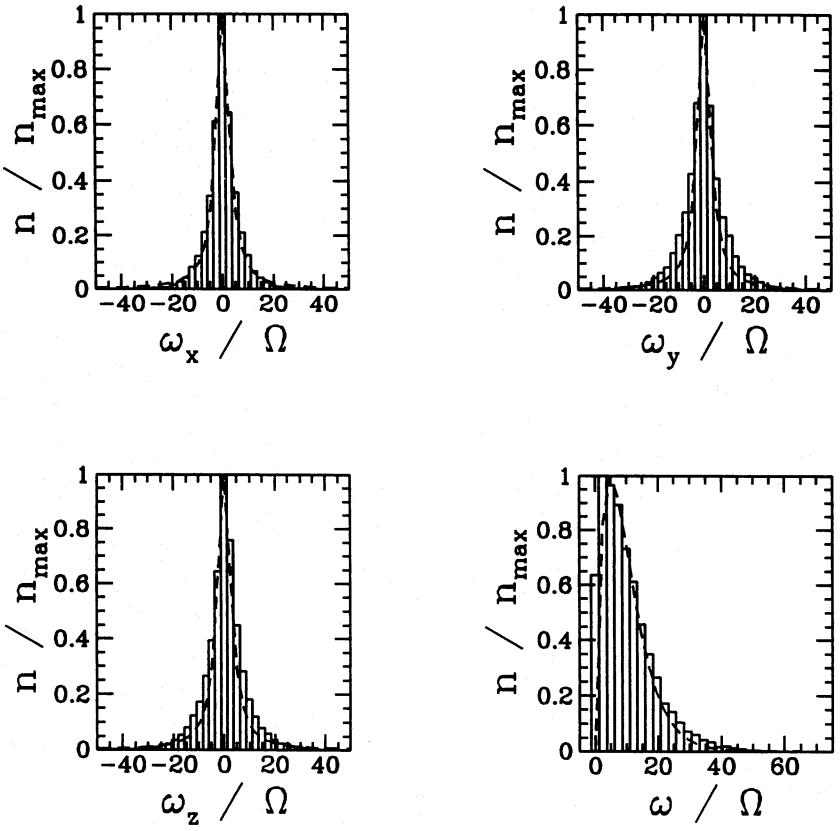

Figure 23. Spin distributions for model (vi.6). The dashed curves for ω_x, ω_y, and ω_z are Lorentzians, while the curve for ω (bottom right) is of the form $\omega e^{-\omega}$. Though impossible to discern by eye, the ω_z distribution is centred slightly off zero, with $\overline{\omega_z} \sim 0.2$.

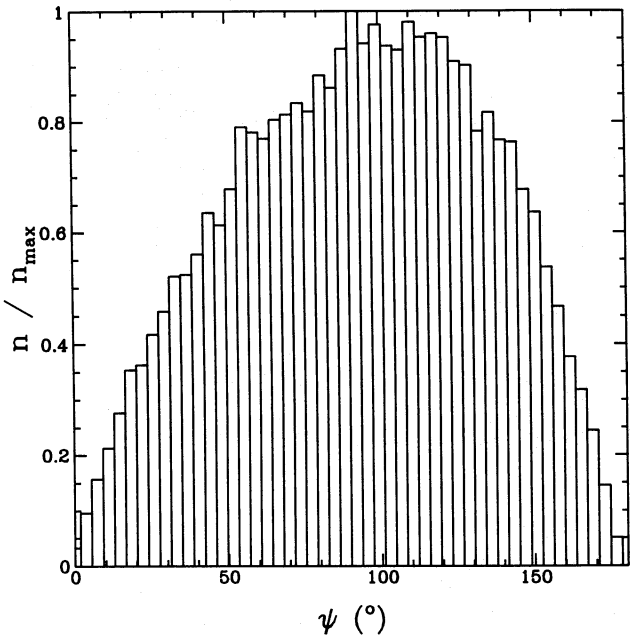

Figure 24. Obliquity distribution for model (vi.6). The FWHM is approximately 120°, or 2/3 of the complete range. On average, the spins of the particles are slightly retrograde.

model. These problems can only be addressed, however, with larger box sizes, again necessitating much larger values of N to test models with comparable density.

4 CONCLUSIONS

New simulations of Saturn's B ring performed using a modified version of `box_tree` have been presented. The code successfully incorporates particle self-gravity, size distributions, and spin, thereby extending the original work of WT. The most important changes to `box_tree` involved improving the time-step formulae and the collision detection techniques, to allow accurate treatment of collisions under close-packed and strong gravity conditions. Comparisons with WT models were presented and showed excellent agreement overall. Improved detail allowed a closer look at layering phenomena. Extensions into the self-gravity and small size distribution regimes showed behaviour similar to the earlier models, and there was still no evidence for overall viscous instability. Larger size ranges at moderate optical depth gave rise to aggregate formation and gravitational wakes, also seen in similar simulations by Salo. The most realistic simulation so far (ΔR = 0.2–5 m, τ = 1) was presented, and also formed density transients. Since *all* size range models showed the rapid development of some form of association, it must be concluded that such systems strongly favour aggregate formation on very short time-scales (less than one revolution), and this may help explain the non-uniformities seen in Saturn's outer rings. It should be noted that the wake lengths in these local simulations may be limited by the choice of box size. Finally, particle spins in these later models were found to lie inside a rotational energy equipartition envelope at equilibrium and were retrograde on average in the local frame, though the particles generally had a large spread in obliquities.

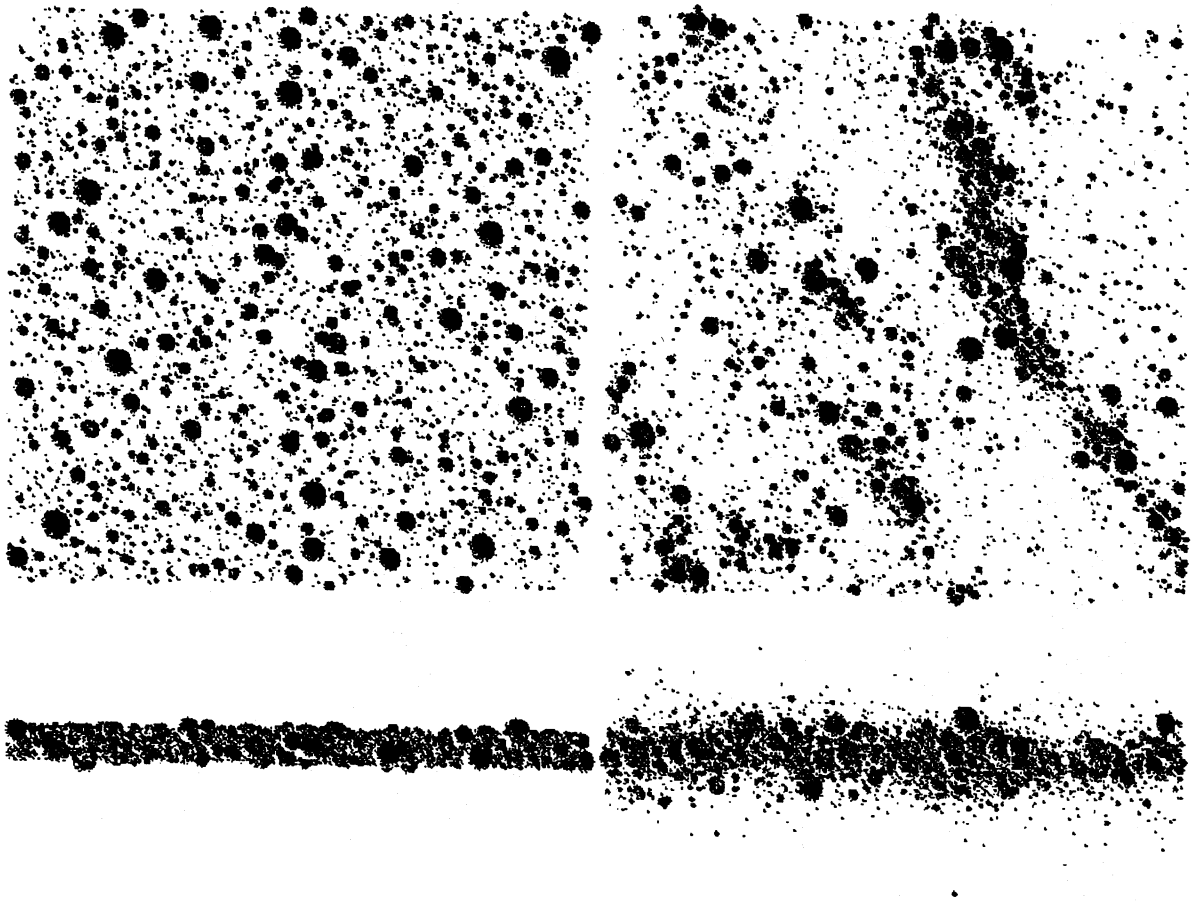

Figure 25. Views of model (vi.6) at time $t = 0$ (left) and $t = 3$ (right), looking down on the z-plane (top) and along the y-axis (bottom). Notice the symmetry in the starting conditions, recalling the mass-weighted balancing about the centre of mass. The evolved system shows several transient density features. Here the box is 170 m on a side.

Even with all the enhancements discussed here, the code still only provides a rough picture of the dynamics in Saturn's rings. Merging (bonding) and fragmentation, for example, were not included and may turn out to play an important role. In particular, frost layers on centimetre-sized particles have been shown to increase dramatically the chance of sticking (Hatzes et al. 1991; Bridges, Supulver & Lin 1994). On a related subject, work is going on to improve the elasticity models of ice particle collisions: recent results suggest that collisions are more elastic than previously thought (thereby increasing the mean equilibrium thickness of the disc and possibly reducing the compactness of aggregates), and it has been found that the *transverse* coefficient of restitution may also be velocity-dependent (Supulver, Bridges & Lin 1994). Other enhancements that need to be made in future include the introduction of non-spherical particles (e.g. ellipsoids with a distribution in axial ratio), although to keep track of position angles and evaluate torque effects correctly will be challenging. Models should also be run for the other main rings, notably A and C.

The most basic improvement needed, however, is a further reduction in CPU expense to allow modelling of the full (known) dynamic range of Saturn's rings, or planetary rings in general, in a practical amount of time. Larger box sizes are also required to guarantee that aggregates and wakes do not interact too much with their ghost images in the sliding box model. Speed improvements can always be achieved by reducing the accuracy of the integration, but this introduces the risk of spurious results. The `box_tree` code is still under development, and the expectation is that as much as another factor of 2 in speed may be achievable for a given accuracy. The code may also benefit from incorporating the new Hermite integrator (Makino & Aarseth 1992), which both simplifies and speeds up particle updates.

The *Cassini* mission to Saturn offers the exciting possibility of testing recent numerical studies of planetary rings directly. To make the most of this opportunity, it is important that as many improvements as possible be made to existing techniques. Some basic refinements have already been mentioned, but there are also many aspects of existing models that need to be explored further in order to determine the best approach towards future development. Particle aggregates in particular merit much further study: the maximum aggregate size needs to be determined, requiring larger scale simulations; a better picture of how the aggregates form and dissolve needs to be obtained; and a determination of the role aggregates may play in reducing the rate of angular momentum transport is also needed. As computing facilities improve, these problems will become increasingly easier to address.

As has happened in the past, it is hoped that the develop-

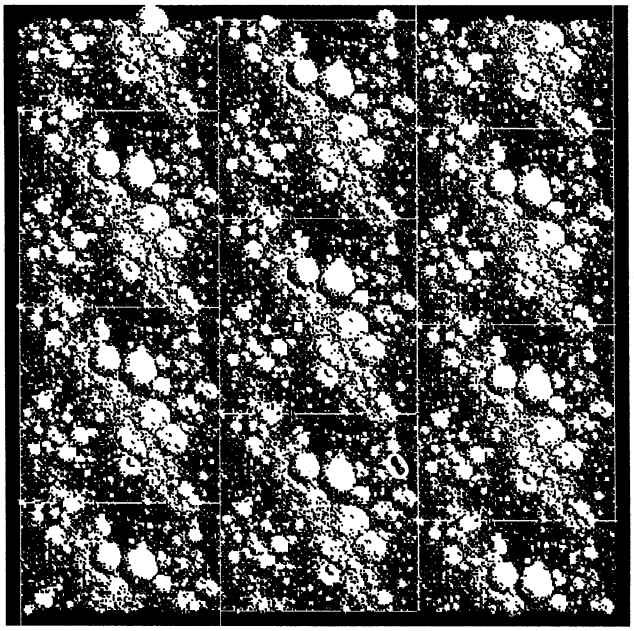

Figure 26. View looking down the z-axis at model (vi.7) after one quarter of an orbit. The view includes the ghost boxes, each of size 50 m. The optical depth is unity. A transient density feature is already forming; note how it seems to extend beyond the central box.

ments made here in studying planetary rings will also benefit the study of Solar system dynamics in general.

ACKNOWLEDGMENTS

The author thanks S. J. Aarseth, D. N. C. Lin, S. Tremaine, and H. Salo for helpful discussion and technical assistance during the preparation of this paper. Also much appreciated was help with TEX and SM from P. Tribble, and comments from G. F. Lewis. The author is indebted as always to the Institute of Astronomy, Cambridge for providing the computing facilities for this project. This work was supported by a Commonwealth Scholarship Award administered through the British Council.

REFERENCES

Aarseth S. J., 1985, in Brackill J. U., Cohen B. I., eds, Multiple Time Scales. Academic Press, New York, p. 377
Aarseth S. J., Lin D. N. C., Palmer P. L., 1993, ApJ, 403, 351
Araki S., 1991, Icarus, 90, 139
Araki S., Tremaine S., 1986, Icarus, 65, 83
Barnes J., Hut P., 1986, Nat, 324, 446
Beaugé C., Aarseth S. J., Ferraz-Mello S., 1994, MNRAS, submitted
Bridges F. G., Hatzes A., Lin D. N. C., 1984, Nat, 309, 333
Bridges F. G., Supulver K. D., Lin D. N. C., 1994, Icarus, submitted
Burns J. A., Showalter M. R., Morfill G. E., 1984, in Greenberg R., Brahic A., eds, Planetary Rings. The University of Arizona Press, Tucson, Arizona, p. 200
Cuzzi J. N., Lissauer J. J., Esposito L. W., Holberg J. B., Marouf E. A., Tyler G. L., Boischot A., 1984, in Greenberg R., Brahic A., eds, Planetary Rings. The University of Arizona Press, Tucson, Arizona, p. 73
Goldreich P., Tremaine S., 1978, Icarus, 34, 227
Hatzes A. P., Bridges F., Lin D. N. C., Sachtjen S., 1991, Icarus, 89, 113
Hernquist L., 1987, ApJS, 64, 715
Julian W. H., Toomre A., 1966, ApJ, 146, 810
Makino J., Aarseth S. J., 1992, PASJ, 44, 141
Petit J. M., Hénon M., 1987, A&A, 173, 389
Richardson D. C., 1993, MNRAS, 261, 396 (Paper I)
Salo H., 1991, Icarus, 90, 254 (also Erratum, Icarus, 92, 367)
Salo H., 1992a, Icarus, 96, 85
Salo H., 1992b, Nat, 359, 619
Supulver K. D., Bridges F. G., Lin D. N. C., 1994, Icarus, submitted
Ward W. R., 1984, in Greenberg R., Brahic A., eds, Planetary Rings. The University of Arizona Press, Tucson, Arizona, p. 660
Wisdom J., Tremaine S., 1988, AJ, 95, 925 (WT)

This paper has been produced using the Blackwell Scientific Publications LATEX style file.